

**Product Development Team  
for  
Advanced Weather Radar Techniques  
Quarterly Report – 3<sup>rd</sup> Quarter FY 04**

**04.6.2 Polarization and Frequency Diversity**

*Algorithms based on polarimetry will meet the aviation needs for information about the volumetric extent of hail, freezing rain, snow, and icing conditions, as well as non-hydrometeor scatterers. The biggest potential payoff is enhanced data quality. For all practical purposes, polarimetric techniques will eliminate problems associated with sea-clutter, ground clutter, AP, and biological scatterers.*

**a) Current Efforts**

**(NSSL):**

Ground-level work began on the integration of numerical model thermodynamic data into the polarimetric Hydrometeor Classification Algorithm (HCA). Although the HCA does an excellent job overall at discriminating hydrometeor types, there exists some overlap between the polarimetric signatures of rain and snow, particularly in light precipitation. The problem becomes particularly acute when there is no “bright band” snow melt signature to aid in the discrimination. Thermodynamic data from numerical models may be input to help in these important situations.

The Rapid Update Cycle (RUC) model is being used early in this effort, and KOUN polarimetric radar data collected during the winter storm of 3-4 December 2002 is being used as a test case. This storm produced a wide variety of precipitation types (Fig. 1). The RUC output of freezing level height (Fig. 2) showed a sharp variation across the area, with heights ranging from 300 to 3000 gpm.

Significant work has also been performed concerning chaff discrimination, which can be a significant problem for many regions. A report on this activity is contained in Appendix 1.

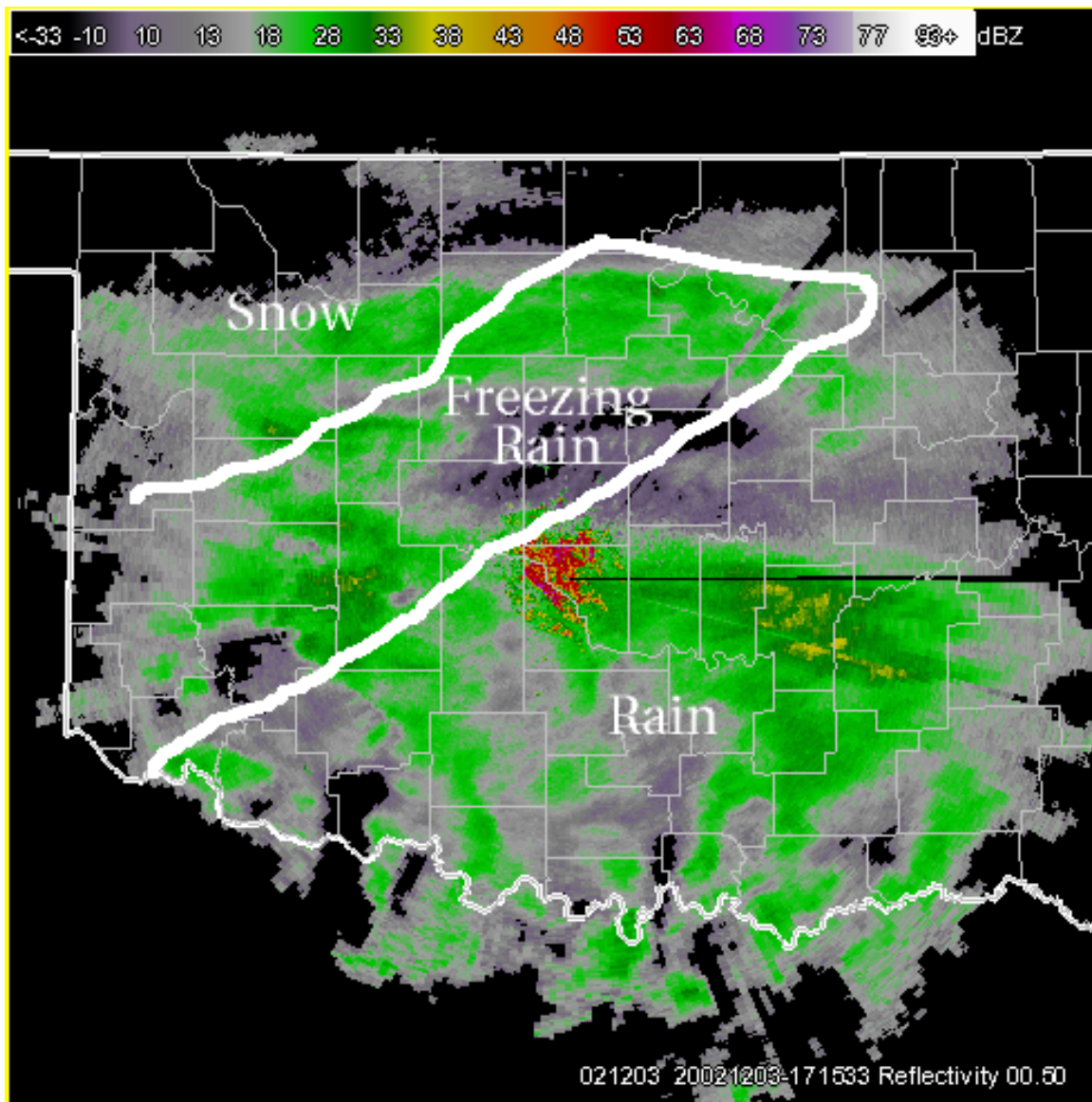


Figure 1. KOUN reflectivity and reported surface precipitation type, 3 December 2002 at 1715 UTC.

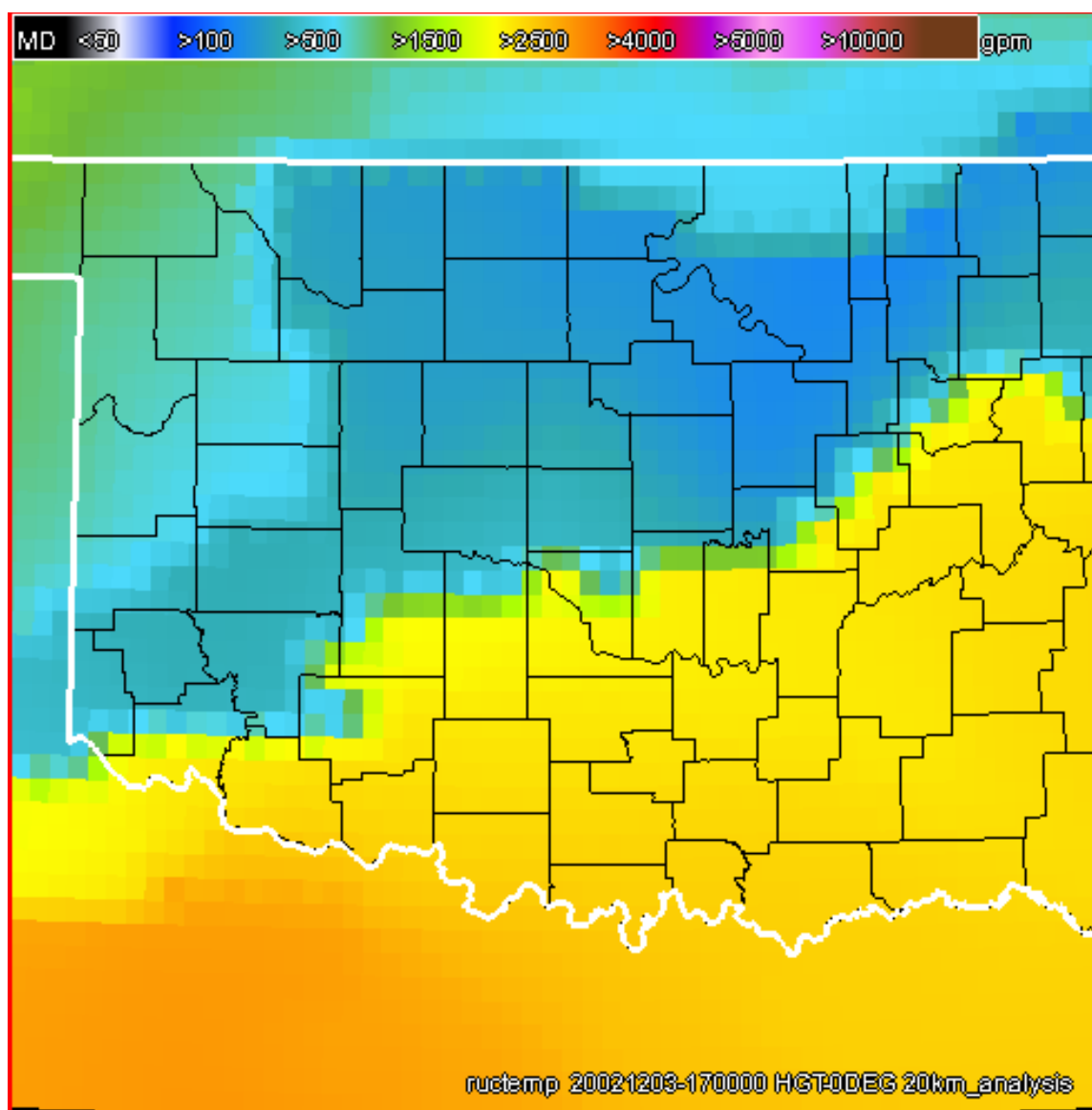


Figure 2. Rapid Update Cycle model depiction of freezing level height, 3 December 2002 at 1700 UTC

Progress has also been made in the identification of radar bright-band signatures in polarimetric data. While the FAA has little interest in rainfall estimation (which is dependent upon properly identifying bright band characteristics) Properly characterizing the bright band is important for rain-snow discrimination within the hydrometeor classification algorithm (HCA). A draft of a conference paper discussing these results is contained in Appendix 2.

### (NCAR):

Tasks 04.6.2.6 and 04.6.2.12: Hydrometeor classification algorithm/hail Detection.

An evaluation of several methods for detecting hail with polarimetric radar measurements has been conducted and a report is being written. Figure 3 presents

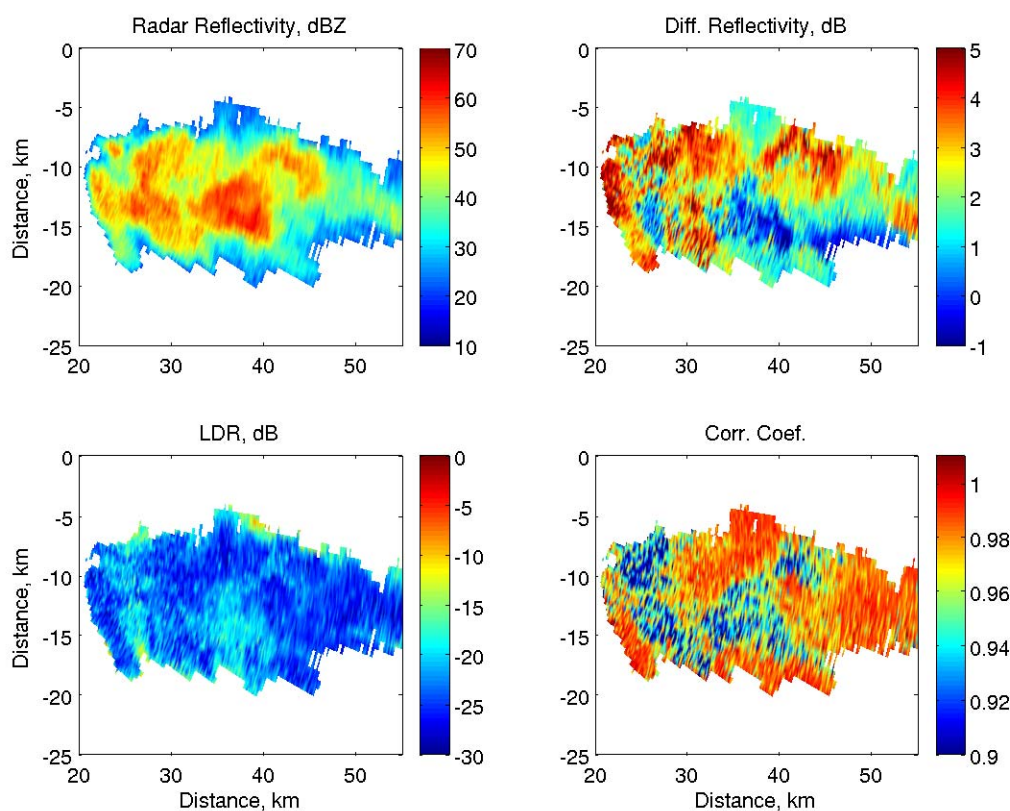


Figure 3. Radar measurements at 0041 UTC, 13 June 2002 from a hailstorm. Radar reflectivity, differential reflectivity, linear depolarization ratio, and correlation coefficient are shown.

polarimetric measurements for a hail-producing storm complex observed in Oklahoma on 13 June 2002. Measurements of radar reflectivity, differential reflectivity, linear depolarization ratio, and correlation coefficient are shown. All measurements respond to the presence of hail. Hail regions are characterized

by high reflectivity and relatively low differential reflectivity, high linear depolarization ratio, and low correlation coefficient.

Figure 4 shows radar reflectivity and hail designations made with the hail

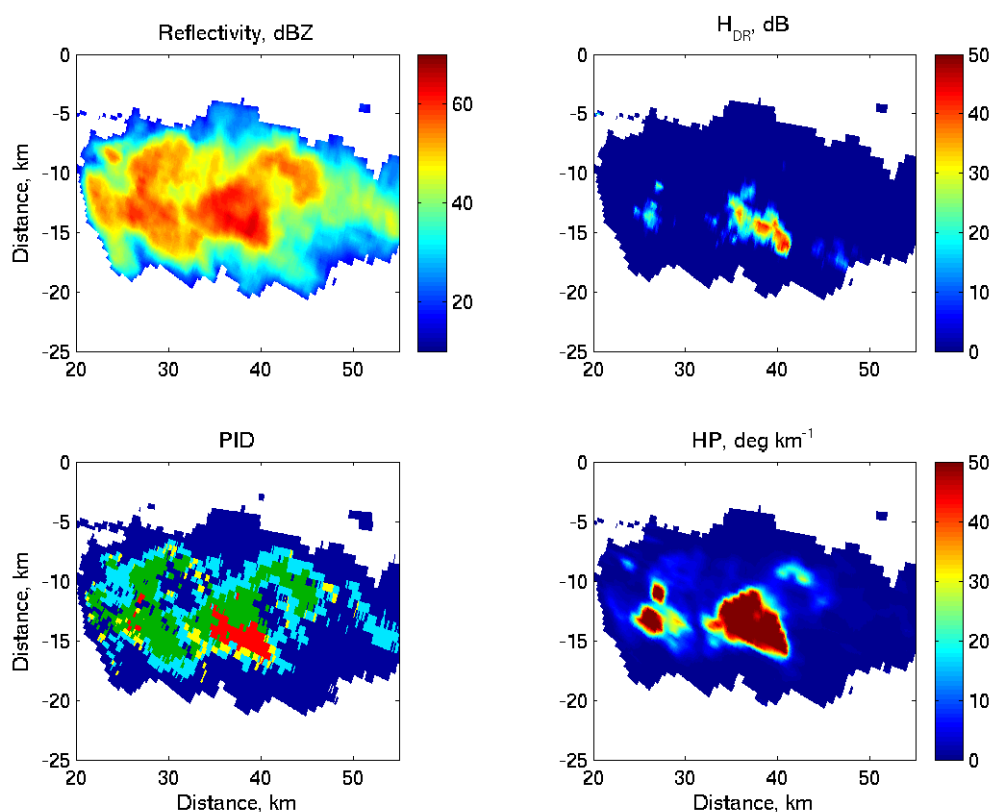


Figure 4. Radar reflectivity (slightly smoothed) and hail designations made with potential algorithms for the data set in Fig. 1. PID classifications are for hail (red) and hydrometeor mixtures: graupel-hail (yellow), rain-hail (green), and graupel-rain (light blue).

parameter ( $H_{DR}$ ) of Aydin et al. (JCAM, 1986), NCAR's hydrometeor classification algorithm (PID), and a new parameter (HP) based on the consistency among measurements of reflectivity, differential reflectivity, and differential propagation phase. The HDR and HP algorithms are not designed to “predict” size, but both size and the probability of hail tend to increase as parameter values increase. The hydrometeor classification algorithm (PID) designations show a core region of hail (in red) with adjacent regions of graupel-hail (yellow) and rain-hail (green). There is a surrounding region of graupel-rain (light blue). While the designations seem plausible, verification will be difficult. All three algorithms predict hail in the same general locations and offer improvement over reflectivity-based algorithms. There are some significant differences that relate to imposed thresholds and susceptibility to variations in raindrop size distributions.

#### Tasks 04.6.2.7 and 04.6.2.11: Winter storm studies

Rain fell in the WISP04 study area on 4 March 2004 after 2300 UTC as upslope flow developed behind a low pressure center. Temperatures rapidly decreased from 5.5 to 0.3°C at 0100 UTC (5 March). Ice pellets, detected by a 2-D video disdrometer as the temperature dropped, became dominant by 0115 UTC. The precipitation changed to snow (dendrites and irregular shaped aggregates) by 0140 UTC.

Using size distributions derived from disdrometer observations, radar reflectivity was computed. A particle density of 1.0 g cm<sup>-3</sup> was used for the rain period. Reflectivity for the frozen particles was computed by assuming that particles were quasi-spherical and had a density of 0.05 g cm<sup>-3</sup> (Fig. 5). The assumed

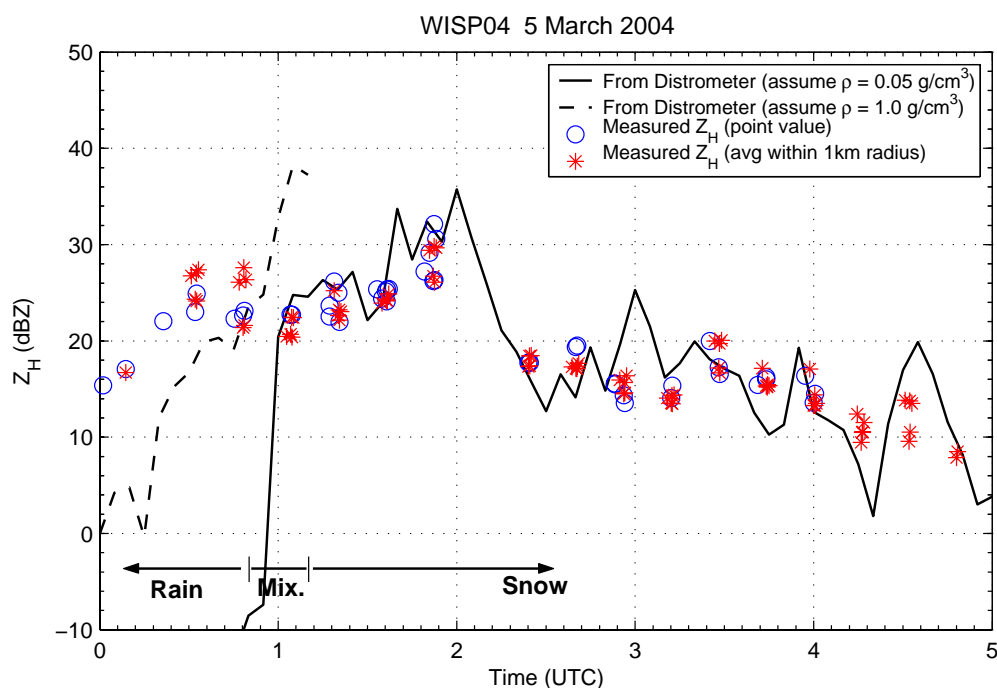


Figure 5. Comparison of radar reflectivity ( $Z_H$ ) as measured by radar and computed from disdrometer observations for the rain/snow event of 5 March 2004. Solid (dashed) line is for the derived  $Z_H$  assuming snow (rain) density of 0.05 g cm<sup>-3</sup> (1.0 g cm<sup>-3</sup>). Radar measurements corresponding to the disdrometer location are represented by open circles. The measurements, averaged over a circular area centered on the disdrometer with a radius of 1 km, are shown with asterisks.

snow density is a representative value based on disdrometer and gauge observations collected from previous winters at the Marshall field site. The comparison is quite good given the many orders of magnitude difference between the radar and disdrometer sampling volumes and the 18 km distance between the

radar and the disdrometer. Additional comparisons for  $Z_H$  and differential reflectivity using varying snow densities are progressing.

c) Problems/Issues

None.

d) Interface with other Organizations

None.

e) Activity Schedule Changes

None.

#### 04.6.3 Circulations

*Particularly violent or long-lived storms tend to possess certain notable qualities, including, for example, mesocyclones. The current WSR-88D algorithms have a very high false alarm rate. Controllers find such high false alarm rates unacceptable. To mitigate this problem, new more robust and reliable circulation detection algorithms will be developed. Algorithms that use circulations to diagnose storm severity or estimate storm longevity will be considerably improved by this work.*

##### a) Current Efforts

Several code changes were made during Q3 to enable testing of different least-squares weighting schemes on radial velocity models of rotation and divergence signatures. Current work focuses on determining the most robust weighting scheme for the kernel used in calculating radial velocity derivatives. Results will be presented at the 11<sup>th</sup> Conference on Aviation, Range, and Aerospace.

Results from this work are likely to be incorporated initially into post-analysis tools for the NWS.

##### b) Planned Efforts

Activity expected to commence in Q2

##### c) Problems/Issues

None.

##### d) Interface with other Organizations

None.

##### e) Activity Schedule Changes

None.



#### **04.6.14 Multi-radar Composites**

*The area for which any arbitrary ARTCC has responsibility likely encompasses the coverage area of several WSR-88D installations. Neither the ROC nor the NWS has plans to treat the various WSR-88D installations as a single network, so there are no existing algorithms that use data from more than one radar. This is a serious limitation, because treating each radar separately leads to ambiguities when the radar data overlap. Currently, the users must independently mitigate these ambiguities, which requires significant knowledge about meteorological radar data and the nature of the algorithms that are run on these data. Aviation users generally do not possess this knowledge, so for the WSR-88Ds to be treated as a network, algorithms and techniques aimed specifically at multiple radar composites must be developed.*

##### **a) Current Efforts**

Activities over Q3 have been very extensive and wide-ranging. The initial capability deadline was missed due to serious hardware and vendor problems, which are outlined in the accompanying report, complete with hyperlinks, attached as Appendix 3. Included in this report are extensive statistics describing the current system performance.

##### **b) Planned Efforts**

For the next quarter, the NCAR REC algorithm will be tested using a variety of cases. The CONUS 3D mosaic system will be further stabilized and optimized. More WSR-88Ds will be integrated into the NMQ mosaic system when they become online. The CONUS 3D mosaic data will be provided to the AWRP users as requested.

##### **c) Problems/Issues**

Hardware failures and problems were encountered during the implementation of the NMQ 3D mosaic system. The problems resulted in the delay of deliverable 04.6.14.E8, "Delivery of NetCDF national 3-D mosaic data sets to PDT partners at NCAR and FSL," from 1 May to 30 June 2004.

The 4D dynamic grid development (task 04.6.14.12) will be postponed to later years (2006 and later) due to several higher priority tasks including gap-filling below the lowest radar beams, reflectivity QC, integration of TDWR data in the CONUS 3D mosaic, etc. Another higher priority task is the creation of 3D mosaic grid for history events as requested by other PDTs.

##### **d) Interface with other Organizations**

Discussions with the CW PDT and the MD&E PDT resulted in a couple of enhancements in the 3D mosaic. One is to distinguish regions of "no radar coverage" and "no echo but with radar coverage" in the 3D reflectivity mosaic. Another is to generate a 2D "lowest available reflectivity observations to the

ground” field. The “no echo” versus “no coverage” flags and the new 2D reflectivity products has been implemented in the NMQ 3D mosaic using two different flags (“-99” for “no echo” and missing value for “no coverage”). The hybrid scan reflectivity product and the height associated with the hybrid scan reflectivity are generated, which can provide information about the radar observations closest to the ground.

e) Activity Schedule Changes

None.

#### 04.6.15 WARP Activities

*The WARP is integral to AT controller displays. Warp is significant in that it shifts the burden of displaying weather radar returns to an instrument specifically designed as a weather radar: the WSR-88D. However, due to the nature of its mission and hardware, the WSR-88D cannot take the same approaches to data quality control as do the long-range L-band radars currently used by ATC. New approaches to data quality control need to be developed so the users have confidence in the weather data products displayed to them.*

##### a) Current Efforts

ORPG AP mitigated products contain a systematic problem of reducing maximum reflectivity values across the entire reflectivity field. However, recent results have shown that a simple correction to the AP mitigation scheme completely eliminates this problem. This solution was presented at the WARP National Working Group Meeting in Norman, OK May 11th-13th. The presentation was enthusiastically received and as a result, an immediate effort is being made to have the modification included within a future build release of ORPG software. Members of the WARP National Working Group expressed interest in viewing additional case studies with the modification to the AP mitigation technique. Test cases from the ongoing WARP ECP 20 Mosaic Generation Algorithm Evaluation will be used for additional examination.

The AP mitigation technique contains 17 adaptable parameters that have been optimally tuned to remove AP while preserving the integrity of precipitation data. However, it is possible the adaptable parameter set may become sub-optimal when using the new modification, which bypasses the use of a median filter in appropriate data regions. Thus, several AP case studies are being re-examined using the new modification while varying the adaptable parameter set in the same manner as found in Smalley and Bennett (2001).

Figures 6-9 show an AP case from May 25, 1994 surrounding the Amarillo, TX WSR-88D (KAMA) radar. Extensive AP exists (Figure 6a) and the AP mitigation technique proves effective at removing the unwanted clutter (Figure 6b). The new correction is able to preserve the true magnitude of reflectivity in the precipitation region southeast of KAMA while remaining efficient at removing AP (Figure 6c). Figure 7 is a recreation of Figure 6 from Smalley and Bennett (2001) showing the improvement in the AP mitigation technique as the adaptable parameter set is optimally tuned. Figure 8 is the same as Figure 7 except the new modification to the AP mitigation technique is employed. Nearly the same progression is seen in the tuning of the adaptable parameter set suggesting that, at least for this AP case, the original optimal adaptable parameter set may indeed still be optimal when disallowing median filtering in precipitation regions

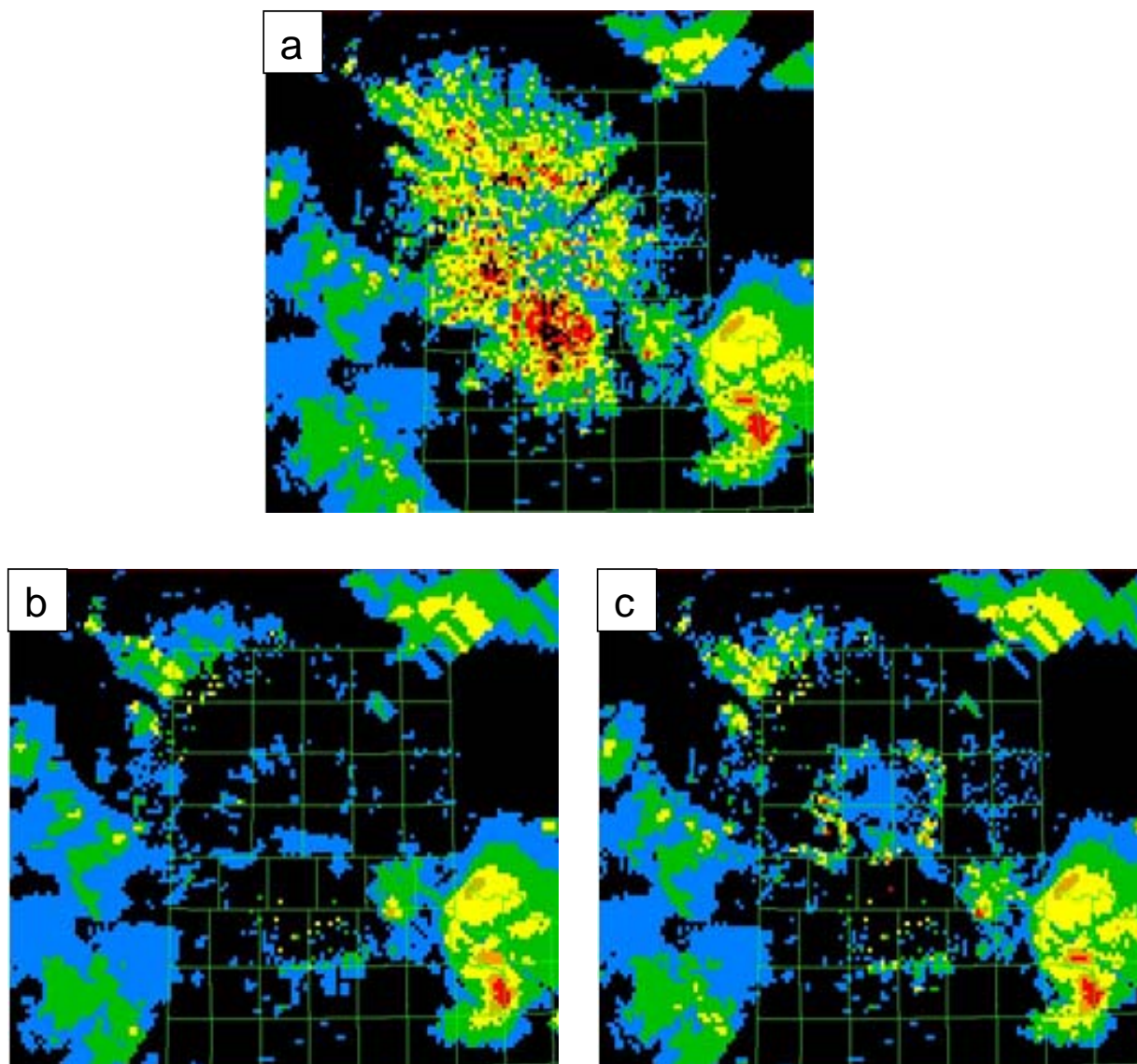


Figure 6. AP case on May 25, 1994 surrounding the Amarillo, TX WSR-88D (KAMA) radar. a) AP removal is not used, b) AP removal used with median filter across entire image, and c) AP is removed and median filter is only used in clutter regions.

b) Planned Efforts

Continue investigation of data quality issues as pertains to WARP applications.

c) Problems/Issues

None.

d) Interface with other Organizations

None.

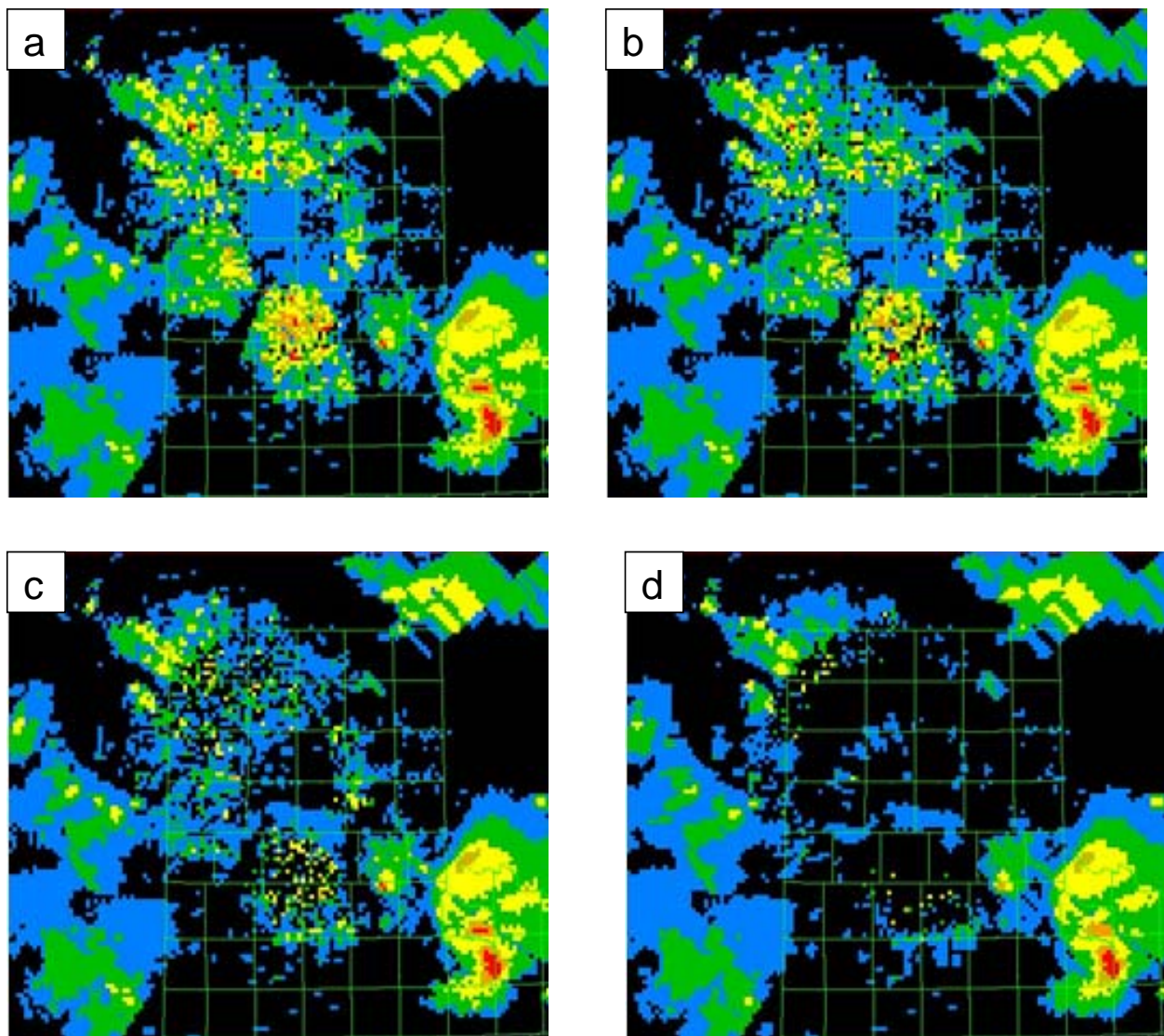


Figure 7. Reproduction of Figure 6 of Smalley and Bennett (2001). The AP mitigation technique is applied (using median filtering across the entire image) using four different adaptable parameter sets: a) original set when the AP technique was first implemented in ORPG composite reflectivity products, b) "MIT/LL," c) "Min. dBZ + Incr. Dop.," and d) the current and optimal set.

#### e) Activity Schedule Changes

None.



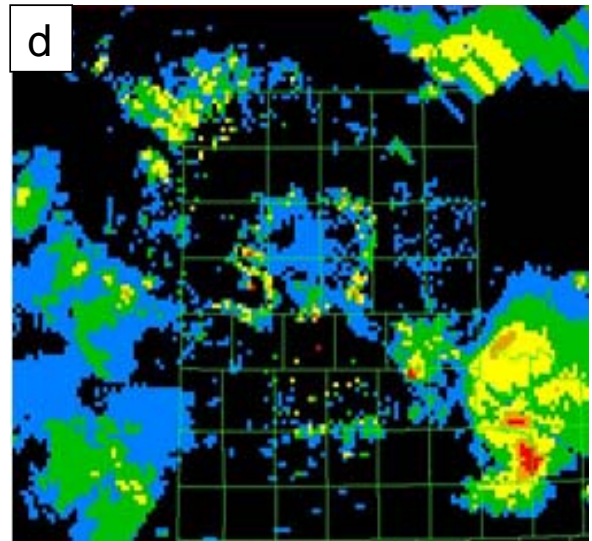
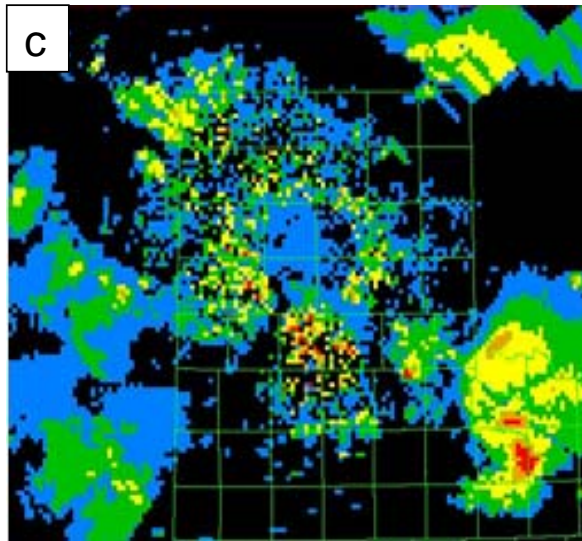
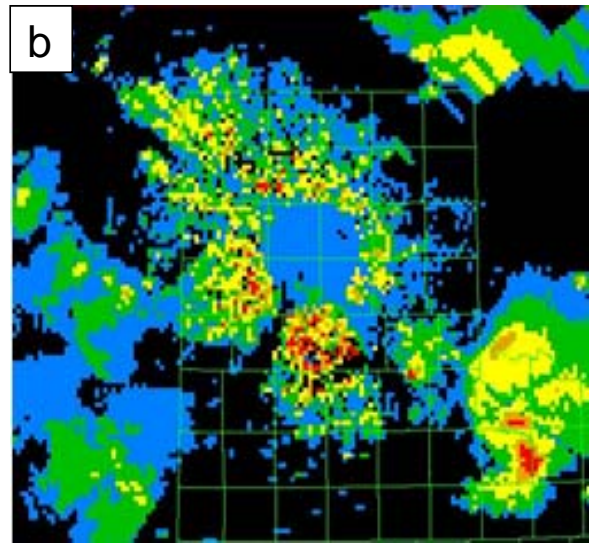
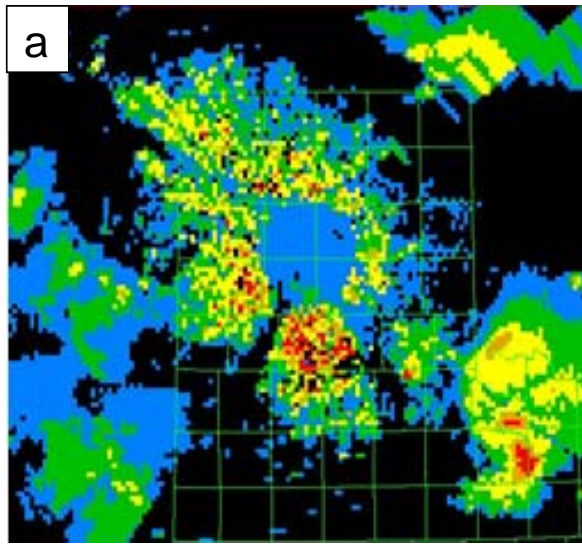
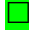


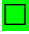











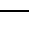
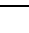



Figure 8. Same as Figure 7 except the new modification to the AP technique is used so that median filtering is not used within precipitation regions.

**Q3 FY 04**  
**Status of Advanced Weather Radar Techniques PDT Deliverables**

**Legend:**  Task proceeding on schedule;  Task complete;  Task incomplete and overdue.

AWRT Deliverable and Related Task	Lead Org	Due	Stat	Comment
04.6.2.1 (Polarization) Chaff identification	NSSL	31/04/04		Start 01/10/03
04.6.2.2 (Polarization) HCA: Wx vs. non-Wx	NSSL	30/09/04		Start 01/10/03
04.6.2.3 (Polarization) Single-pol time series for biological scatterer discrimination	NSSL	30/09/04		Start 01/10/03
04.6.2.4 (Polarization) $\rho_{hv}$ vs. LDR for rain/snow discrimination	NSSL	30/06/04		Start 01/10/03
04.6.2.5 (Polarization) HCA development using JPOLE data set	NSSL	31/03/04		Start 01/10/03
04.6.2.6 (Polarization) HCA verification	NSSL	30/05/04		Start 31/03/03
04.6.2.7 (Polarization) Complete winter storm cases from 1997 and 2002.	NSSL	30/09/04		Start 01/10/03
04.6.2.8 (Polarization) JPOLE Phase I Data Collection: Plan Cold-Season	NSSL	30/09/04		Start 01/10/03
04.6.2.9 (Polarization) dual-pol, dual- $\lambda$ , disdrometer, radiometer, vis, snowfall vs. in situ icing rate	NCAR	30/09/04		Start 01/10/03
04.6.2.10 (Polarization) Examine icing events from IMPROVE field experiment	NCAR	30/09/04		Start 01/10/03
04.6.2.11 (Polarization) use microphys obs in winter storms to improve QPE and visibility	NCAR	30/09/04		Start 01/10/03
04.6.2.12 (Polarization) Verify NCAR HCA on WSR-88DP prototype (KOUN)	NSSL	30/09/04		Start 01/10/03
04.6.2.13 (Polarization) Use KOUN data and OUN soundings to verify freezing level algorithm	NCAR	30/09/04		Start 01/10/03
04.6.3.1 (Circulation Detection) Continue LLSD development	NSSL	30/09/04		Start 01/10/03
04.6.3.2 (Circulation Algorithm) LLSD case verification/analysis	NSSL	30/09/04		Start 01/10/03
04.6.14.1 (Multi-Radar) Present/explain 3D grid to users; obtain input from users	NSSL	31/12/03		Start 01/10/03

04.6.14.2 (Multi-Radar) Improve/develop 3D algorithms based on user feedback	NSSL	30/09/04	<input checked="" type="checkbox"/>	Start 1/1/04
04.6.14.3 (Multi-Radar) Generate/disseminate 3D gridded data over CIWS region	NSSL	Quarterly	<input checked="" type="checkbox"/> <input checked="" type="checkbox"/> <input checked="" type="checkbox"/> <input type="checkbox"/>	Start 01/10/03
04.6.14.4 (Multi-Radar) Maintenance/update mosaic coding/ingest	NSSL	30/09/04	<input type="checkbox"/>	Start 01/10/03
04.6.14.5 (Multi-Radar) Develop computational strategies/run-time scripts for 3D CONUS grid	NSSL	31/12/03	<input type="checkbox"/>	Start 01/10/03
04.6.14.6 (Multi-Radar) Prepare reference files and background data for National Mosaic	NSSL	1/02/04	<input checked="" type="checkbox"/>	Start 01/12/03
04.6.14.7 (Multi-Radar) Develop/prototype system for real-time CONUS 3D mosaic	NSSL	1/04/04	<input checked="" type="checkbox"/>	Start 01/03/04
04.6.14.8 (Multi-Radar) Deliver NETCDF files of CONUS 3D grid	NSSL	1/05/04	<input checked="" type="checkbox"/>	Start 01/10/03
04.6.14.9 (Multi-Radar) Implement NCAR REC algorithm for CONUS 3D grid preprocessing	NSSL	30/09/04	<input type="checkbox"/>	Start 30/06/04
04.6.14.10 (Multi-Radar) Test NCAR REC	NSSL	30/06/04	<input checked="" type="checkbox"/>	Start 01/01/04
04.6.14.11 (Multi-Radar) 4D CONUS grid development	NSSL	30/06/04	<input type="checkbox"/>	Start 01/01/04
04.6.14.12 (Multi-Radar) Test 4D CONUS grid prototype on 88D and TDWR	NSSL	30/09/04	<input type="checkbox"/>	Start 1/07/04
04.6.15.1 (WARP Support) Investigate Product 67 problems	NSSL	31/12/04	<input checked="" type="checkbox"/>	Start 01/10/03
04.6.14.6 (WARP Support) Develop options for fixing Product 67	NSSL	30/04/04	<input checked="" type="checkbox"/>	Start 01/01/04
04.6.15.1 (WARP Support) Evaluate Engineering Change Proposal 20	NSSL	30/09/04	<input type="checkbox"/>	Start 01/05/04

\* Due date revised thru AWRP POC.



## **Polarimetric Properties of Chaff**

Dusan S. Zrnic<sup>1</sup> and Alexander V. Ryzhkov<sup>2</sup>

1) National Severe Storms Laboratory, Norman OK

2) Cooperative Institute for Mesoscale Meteorological Studies, CIMMS, University of  
Oklahoma, Norman, OK

## ABSTRACT

Chaff contaminates estimates of precipitation amounts hence it is important to remove (or censor) its presence from the fields of radar reflectivity. It is demonstrated that efficient and direct identification of chaff is possible with polarimetric radar. Specifically considered are horizontal and vertical polarization basis and covariances of corresponding returned signals. Pertinent polarimetric variables are copolar correlation coefficient, differential reflectivity, and linear depolarization ratio. Two models are used to compute the expected values of these variables. In one, chaff is approximated with a Hertzian dipole and in the other with a thin wire antenna. In these models chaff is assumed to have a uniform distribution of flutter angles (angle between the horizontal plane and chaff axis). The two models produce nearly equivalent results. Also shown are polarimetric signatures of chaff observed in the presence of precipitation. Inferences about chaff's orientation are made from comparisons between measured and observed differential reflectivity and cross correlation coefficient.

## 1. Introduction

Chaff is made of aluminum coated thin fibers and is released by the military to create widespread echoes and thus confuse non-cooperating tracking radars.

To maximize backscattering cross section chaff length is chosen to equal one half the radar wavelength. As predominant wavelengths for military surveillance and tracking are 3, 5, and 10 cm the standard chaff lengths are 1.5, 2.5, and 5 cm. Because chaff is employed by the military as part of routine training in the USA, it is often observed as echoes on weather radars (Maddox et al. 1997). Although the reflectivity is relatively weak it is sufficient to contaminate precipitation estimates (Vasiloff and Struthwolf 1997, see the URL at <http://www.wrh.noaa.gov/wrhq/97TAs/TA9702/ta97-02.html>). Examples abound in Western US whereby chaff is imbedded in precipitation (opus cited) or coexist next to precipitation echoes (Ziegler et al. 2001, Brandt and Atkin 1998, <http://www.wrh.noaa.gov/wrhq/98TAs/9804/index.html>). Thus it is desirable to recognize returns due to chaff and censor these from precipitation products.

It has been argued (Zrnic and Ryzhkov 1999) that polarimetric radar offers simple and effective way to identify chaff. The argument is rooted in common sense logic and experimental evidence gained with circularly polarized radars (Brooks et al. 1992). Polarimetric signatures of chaff in linear horizontal and vertical basis have not been reported. Moreover, because chaff is a nuisance (as far as observation of weather is concerned), little or no theoretical results about its polarimetric properties are available. In few years the National Weather Service will add polarimetric capability to its network of WSR-88D radars. Therefore it will soon be possible to have a simple automated procedure for censoring chaff. Our purpose herein is to present scattering models of

chaff that capture the essential polarimetric properties as well as some data to support these properties.

In laminar airflow, chaff is mostly horizontally oriented and slowly falls with respect to air. Turbulence and differential air motion will cause wobbling. In either case differential reflectivity  $Z_{DR}$  is expected to be relatively large. Linear depolarization ratio  $L_{DR}$  will increase compared to the value in precipitation and the cross correlation between copolar returns  $\rho_{hv}$  will decrease. These polarimetric variables do not depend on the absolute values of returned power (i.e., backscattering cross section), yet they are the most significant discriminators. It is the insensitivity to cross-section that simplifies model development.

Two simple models for computing polarimetric properties of chaff come to mind. In one the chaff is approximated with the Hertzian Dipole so that standard formulas (i.e., for prolate spheroids with induced field along the axis and no field perpendicular) could be applied to compute the elements of the covariance matrix. This approximation is applicable for chaff lengths much shorter than the wavelength. But, for polarimetric variables that are independent of concentration and backscattering cross section we show that the model can be extended to half wavelength sizes.

A more realistic approach is to model chaff as thin cylindrical antenna and apply standard formulas to obtain scattering coefficients. This second approach is also explored herein. Then, once the scattering coefficients are determined, the geometrical transformations as done for the spheroids (Bringi and Chandrasekhar 2001, Ryzhkov 2001) can be used for computation of the polarimetric variables.

The underlying assumption in our models is that chaff does not clump and does not flex on the way to the ground. To compute the fields of flexing and or clumping chaff two steps are needed. First a physical model is required to describe the flexing and/or clumping geometry. Then a numerical solution, such as discrete dipole approximation (Evans and Vivekanandan 1990) should be applied to this geometry to obtain the scatter coefficients. Because the extent of clumping and/or flexing is not known we consider only rigid chaff without clumps for which the thin antenna model is very well suited.

Both our models can be applied to determine chaff concentration  $N_o$  within the resolution volume from a relation between volume reflectivity  $\eta$  ( $\text{m}^2\text{m}^{-3}$ ) and specific differential phase  $K_{DP}$ . This is significant for studies of diffusion in the atmosphere (e.g., Hildebrand 1977). Whereas such and similar studies (Martner et al. 1992) relied on resolution volume weighted averages over the chaff field, the polarimetric method allows much finer resolution. It is possible to achieve about a km in the radial direction (sufficient for estimating specific differential phase) and the intrinsic beamwidth dictates the transverse resolution.

## **2. Models**

### *a) Hertzian Dipole*

Patterned after a prolate spheroid, this model in general can be thought of as composed of two orthogonal dipoles. One has fixed orientation along the chaff axis, the other is induced perpendicular to the axis. The dipole along the chaff axis is dominant and will be used initially to compare this simple model with a thin wire model. This model is strictly valid for chaff lengths much smaller than the wavelength. Nonetheless it

turns out that its results compare fairly well to the thin wire model. Let the scattering amplitude for the E field along the axis be  $f_a$  and the amplitude for the perpendicular field be  $f_b$ . For a perfect conductor the two amplitudes will be in phase. Therefore without loss of substance we assume these to be real. Then, as shown by Holt and Shepherd (1979) we write the backscattering matrix S

$$S = \begin{bmatrix} (f_a - f_b) \sin^2(\psi) \sin^2(\alpha) + f_b & (f_a - f_b) \sin^2(\psi) \sin(\alpha) \cos(\alpha) \\ (f_a - f_b) \sin^2(\psi) \sin(\alpha) \cos(\alpha) & (f_a - f_b) \sin^2(\psi) \cos^2(\alpha) + f_b \end{bmatrix}. \quad (1)$$

In (1)  $\psi$  is the angle between the axis of chaff and the propagation vector and  $\alpha$  is the canting angle; the equation is valid for Rayleigh scatterers (i.e., small compared to wavelength).

Next we list equations for the components of the covariance scattering matrix which determine the polarimetric variables studied herein. The assumption is that multiple scattering is insignificant, all chaff needles have same size, and there is a distribution of orientation. Following Ryzhkov (2001) the pertinent elements are

$$\begin{aligned} \langle |s_{hh}|^2 \rangle &= \langle |f_b|^2 \rangle - 2\langle (f_b^2 - f_a f_b) A_2 \rangle + \langle |f_b - f_a|^2 A_4 \rangle \\ \langle |s_{vv}|^2 \rangle &= \langle |f_b|^2 \rangle - 2\langle (f_b^2 - f_a f_b) A_1 \rangle + \langle |f_b - f_a|^2 A_3 \rangle \\ \langle |s_{hv}|^2 \rangle &= \langle |s_{vh}|^2 \rangle = \langle |f_b - f_a|^2 A_5 \rangle \\ \langle s_{hh}^* s_{vv} \rangle &= \langle |f_b|^2 \rangle + \langle |f_b - f_a|^2 A_5 \rangle - \langle (f_b^2 - f_a f_b) A_1 \rangle - \langle (f_b^2 - f_a f_b) A_2 \rangle \end{aligned} \quad (2)$$

In these equations the  $A_i$  s are products of sinusoidal functions

$$A_1 = \sin^2(\psi) \cos^2(\alpha)$$

$$A_2 = \sin^2(\psi) \sin^2(\alpha)$$

$$A_3 = \sin^4(\psi) \cos^4(\alpha)$$

$$A_4 = \sin^4(\psi)\sin^4(\alpha) \quad (3)$$

$$A_5 = \sin^4(\psi)\cos^2(\alpha)\sin^2(\alpha)$$

Assume that the chaff is randomly oriented in the horizontal plane (i.e., azimuth angle  $\varphi$  is between 0 and  $2\pi$ ), the radar elevation is 0 deg (a good approximation for surveillance radars), and the angle between axis of chaff and horizontal plane is uniformly distributed from 0 to  $\pi/2 - \theta_I$  (angle  $\theta_I$  is measured with respect to the true vertical). Henceforth the maximum deviation ( $\pi/2 - \theta_I$ ) will be referred to as “flutter angle”. Thus, a probability density function that represents a uniform distribution of orientation within the above prescribed limits is given by

$$p(\theta, \varphi) = \sin(\theta)/[2\pi\cos(\theta_I)]. \quad (4)$$

The following relations between the  $\alpha$ ,  $\psi$  and  $\theta$ ,  $\varphi$  angles

$$\sin(\theta)\cos(\varphi) = \sin(\alpha)\sin(\psi)$$

$$\cos(\theta) = \sin(\psi)\cos(\alpha) \quad (5)$$

$$\cos(\psi) = \sin(\theta)\sin(\varphi)$$

are needed to integrate various terms in equations (2). Two of the equations in (5) are independent, but three are listed for convenience (these are substituted into various integrands).

Next the scattering amplitudes are assumed fixed and the transverse amplitude  $f_b=0$ . Then integration with the prescribed distribution produces the following closed form solutions for the angular moments  $\langle A_i \rangle$ s,

$$\langle A_1 \rangle = \cos^2(\theta_I)/3$$

$$\langle A_2 \rangle = [\sin^2(\theta_I)/6 + 1/3]$$

$$\langle A_3 \rangle = \cos^4(\theta_I)/5$$

$$\langle A_4 \rangle = 3[\sin^4(\theta_l) - 4\cos^2(\theta_l)/3 + 4]/40 \quad (6)$$

$$\langle A_5 \rangle = [\cos^2(\theta_l)/3 - \cos^4(\theta_l)/5]/2$$

These will be used shortly to plot the polarimetric variables  $Z_{DR}$ ,  $\rho_{hv}$ ,  $L_{DR}$ , and the ratio  $(K_{DP})^2/\eta$ . The cross to copolar correlations  $\rho_{xh}$  and  $\rho_{xv}$  are zero for chaff with a random horizontal orientation and zero mean flutter angle.

*b) Thin cylindrical antenna*

In this model chaff is represented as a thin cylindrical antenna of length  $L$  and radius  $a$ . The antenna is illuminated by a plane wave, the angle between the antenna axis and the propagation direction is  $\psi$ , and the electric field, the antenna, and the propagation vector are in common plane. It is accepted practice to assume the following sinusoidal distribution of the induced current along the antenna

$$I(l) = I_m \sin\left[\frac{2\pi}{\lambda}\left(\frac{L}{2} - |l|\right)\right], \quad (7)$$

where  $I_m$  is the maximum value of current (depending on  $\psi$ ), the wave number  $k=2\pi/\lambda$ , and  $l$  is distance to the antenna midpoint. Further, the midpoint also serves as the phase reference.

The antenna impedance, the incident electric field along the antenna  $E_l = E \sin(\psi) \exp[-jkl\cos(\psi)]$ , the current  $I(0)$ , and the distribution (7) satisfy (Jordan and Balmain 1968, eq 14-16)

$$Z_i = -\frac{1}{I^2(0)} \int_{-L/2}^{L/2} E_l I(l) dl. \quad (8)$$



Obviously, the plane wave electric field at the antenna location has a magnitude  $E$ ; harmonic time dependence is assumed (but not explicitly written) for all fields and currents.

Substitution of (7) into (8) relates  $I_m$ ,  $Z_i$ , and  $E$ . Further, values of  $Z_i$  can be computed from a relatively cumbersome formula if the thickness, length, and wavelength of the thin antenna are known (Krauss 1950). The current distribution induced by the incident field produces a field at a range  $r$  (far from the antenna) given by equation (5-81) in (Krauss 1950). After elimination of  $I_m$  the final expression for this electric field is

$$E_\psi = -j \frac{60E\lambda}{rZ_i\pi \sin^2(\pi L/\lambda)} \left[ \frac{\cos[kL \cos(\psi)/2] - \cos(kL/2)}{\sin(\psi)} \right]^2. \quad (9)$$

There are no other field components (the units in (9) are MKS and 60 has units of ohms which come from the characteristic impedance of free space). Therefore, the scattering coefficient  $s_{yy}$  can be obtained by omitting  $-j$ ,  $r$  and  $E$  from equation (9).

$$s_{yy} = \frac{60\lambda}{Z_i\pi \sin^2(\pi L/\lambda)} \left[ \frac{\cos[kL \cos(\psi)/2] - \cos(kL/2)}{\sin(\psi)} \right]^2 \quad (10)$$

Note that the scattering coefficient  $s_{yy}$  is the same for the forward and back direction (because the antenna is axially symmetric). It represents the radiation pattern (amplitude) of the scatterer. The induced electric field perpendicular to the axis will be neglected. Thus, the formalisms developed for dipole model (prolate spheroid) can be directly applied to compute elements of the covariance matrix. It suffice to substitute  $|s_{yy}|^2$  in place of  $f_a^2 \sin^2(\psi)$  so that

$$\langle |s_{hh}|^2 \rangle = \langle \sin^4(\alpha) |s_{yy}|^2 \rangle$$

$$\langle |s_{vv}|^2 \rangle = \langle \cos^4(\alpha) |s_{yy}|^2 \rangle$$

$$\langle |s_{hv}|^2 \rangle = \langle |s_{vh}|^2 \rangle = \langle \sin^2(\alpha) \cos^2(\alpha) |s_{yy}|^2 \rangle \quad (11)$$

$$\langle s_{hh}^* s_{vv} \rangle = \langle \sin^2(\alpha) \cos^2(\alpha) |s_{yy}|^2 \rangle.$$

Integrals in (11) are two-dimensional (over  $\theta$ ,  $\varphi$ ) and no closed form solutions are possible (except in some trivial cases like for  $\theta_l = \pi/2$ ). Hence one resorts to numerical integration.

### c) Results of computations

Next, three polarimetric variables are computed for the two models previously described. These are

$$\begin{aligned} \text{Differential reflectivity} \quad Z_{DR} &= 10 \log(\langle |s_{hh}|^2 \rangle / \langle |s_{vv}|^2 \rangle) \\ \text{Copolar cross correlation coefficient} \quad \rho_{hv} &= \langle s_{hh}^* s_{vv} \rangle / (\langle |s_{hh}|^2 \rangle \langle |s_{vv}|^2 \rangle)^{1/2} \quad (12) \\ \text{Linear depolarization ratio} \quad L_{DR} &= 10 \log(\langle |s_{vh}|^2 \rangle / \langle |s_{hh}|^2 \rangle) \end{aligned}$$

Under the assumption that the induced field transverse to the chaff axis is negligible (as written in eq 11) these three variables are related via

$$L_{dr} = \rho_{hv} (Z_{dr})^{-1/2}, \quad (13)$$

wherein  $L_{dr}$  and  $Z_{dr}$  are expressed in linear units.

The three variables (12) are plotted in figures 1, 2, and 3 for both models. The fluttering angle in these figures is between the chaff axis and the horizontal plane (equal to  $\pi/2 - \theta_l$ ). Also three lengths of chaff are used in the antenna model. The choice is such that for 10 cm wavelength radar, chaff needles are 5, 2.5, and 1.5 cm; these are standard chaffs for confusing radars with wavelengths of 10 cm, 5 cm, and 3 cm respectively. A glaring conclusion is that the difference in  $Z_{DR}$  and  $L_{DR}$  for the two models is insignificant. The difference in the  $\rho_{hv}$  (at small flutter – wobbling) is inconsequential for the purpose of identifying chaff.

Further, practical radars are limited in measurements of these polarimetric variables. For example the minimum  $L_{DR}$  due to coupling through the system is about -30 dB which means that only wobbling by more than about  $\pm 4$  deg could be discerned (Fig 3). A more stringent limit to both estimates of  $L_{DR}$  and  $Z_{DR}$  is the receiver noise power that would overwhelm the weaker signal. Bias in these estimates due to receiver noise can be eliminated but the variance at low signal to noise ratios increases.

Comparison of the three variables from the two models suggests that the simple dipole is quite adequate to explain the dependence on the wobbling (fluttering) angle. This dependence is mostly due to the orientation of the chaff needles (or dipole moments) and is little affected by the angular dependence of the scattering coefficients. This independence is expected for chaff lengths that produce one lobe of the backscatter pattern. Although this lobe is sharper for the thin antenna than the dipole, it makes little difference to the variables on the average.

The rather large values in  $Z_{DR}$  predicted for flutter angles between 0 and 40 deg require some explanation. Without direct measurement we speculate that four factors at play might prevent such large values. One, it could be that natural wobbling is larger. Two, induced field transverse to the chaff axis might be present. Three, there could be some flexing of the chaff as it falls. Four, the weaker signal (in the vertical channel) is below noise level.

The antenna model does have an advantage if one is interested in the backscattering cross section or specific differential phase. It can predict fairly well the magnitudes of the scattering coefficients provided the size of chaff is known. With this knowledge one could possibly determine the number density of chaff from the reflectivity

factor and or specific differential phase. But there are no compelling reasons to estimate chaff density unless it could be used to separate its contribution from precipitation in the same resolution volume. At the moment this is a remote possibility, whereas censoring chaff is waiting to be applied on the future polarimetric WSR-88D.

### 3. Chaff Density

Next we present formalism for computing chaff density. This can be achieved by measuring the specific differential phase  $K_{DP}$  and volume reflectivity.

By definition for the Hertzian dipole model of chaff

$$K_{DP} = 180 \lambda f_a N_o (<A_2> - <A_1>)/\pi = 180 \lambda f_a N_o \sin^2(\theta_l)/(2\pi) \text{ (deg m}^{-1}\text{)} \quad (14)$$

where the units for  $\lambda$  and  $f_a$  are meters and concentration  $N_o$  is per  $\text{m}^3$ . Further it is assumed that the imaginary part of  $f_a$  is zero.

In case of a thin antenna the equation becomes

$$K_{DP} = 180 \lambda N_o [<\sin^2(\alpha)|s_{yy}|> - <\cos^2(\alpha)|s_{yy}|>]/\pi. \quad (15)$$

The volume reflectivity  $\eta$  (at horizontal polarization) is related to the scattering coefficients by

$$\eta = 4\pi N_o <|s_{hh}|^2>. \quad (16)$$

For the Hertzian dipole substitute  $<|s_{hh}|^2> = |f_a|^2 <A_4>$  in (16), square (14) and divide with (16) to obtain

$$\frac{(K_{DP})^2}{\eta} = \frac{2025 \sin^4(\theta_l)}{\pi^3 [\sin^4(\theta_l) - 4 \cos^2(\theta_l)/3 + 4]} \lambda^2 N_o. \quad (17)$$

Clearly this ratio depends on the radar wavelength, flutter angle  $(\pi/2 - \theta_l)$ , and concentration. Computations for the thin antenna model require similar substitution but with  $<|s_{hh}|^2>$  from (11) into (16), then squaring (15), and dividing with (16). Note units in

(17) are mks, and  $K_{DP}$  is in ( $\text{deg m}^{-1}$ ). It happens that the result is the same if units of  $K_{DP}$  are changed to the more representative ( $\text{deg km}^{-1}$ ) and  $\eta$  is in ( $\text{mm}^2 \text{m}^{-3}$ ).

Plots of (17) and similar value for the thin antenna (Fig. 4) indicate the multiplying factor (in units of  $\lambda^2 N_o$ ) is relatively insensitive to the chaff length. Further, it changes by less than 20% for small flutter angles ( $< 20$  deg). Thus, in such instances it might be possible to determine chaff's concentration if the return at vertical polarization is sufficiently strong for accurate estimation of  $K_{DP}$ . Similar reasoning might be applied to determine concentration of mono dispersed ice needles.

#### **4. Experimental Data**

On 6 February 2003, a cloud of ice crystals (henceforth, snow band) was observed initially over northwest OK, following a snowfall event. This feature advected southeastward toward Oklahoma City (Fig. 5). At the same time, a chaff "cloud" released from an Air Force base in eastern New Mexico moved across southern Oklahoma.

The reflectivity structures of snow band and chaff look very similar but the polarimetric variables exhibit significant differences. Differential reflectivity of chaff ranges from 0 to 6 dB whereas for snow it is 0 to 3 dB, hence there is overlap of values. The fields of correlation coefficient uniquely identify chaff and separate fairly well snow from ground clutter except in regions where SNR in snow is low (at far distances from the radar, see Fig. 5). Total differential phases of chaff and snow ( $\Phi_{DP}$ ) also differ substantially. The differential phase in region of snow is close to the "system" differential phase (of about  $30^\circ$ ) and exhibits very small spatial fluctuations. In contrast, differential phase of chaff is characterized by significant spatial variations.

More detailed analysis of the histogram of  $\Phi_{DP}$ , prior to radial averaging, in chaff reveals broad maximum at about  $80^\circ$ . This mean value of  $\Phi_{DP}$  might be indicative of the “receiver component” of the “system” differential phase. Indeed, physical considerations indicate that chaff produces zero backscatter differential phase. That is, regardless of the transmitted differential phase between the H and V components each needle reflects a field aligned along its axis. Thus, upon reflection the H and V fields are in phase. Once these fields are transformed into voltages and subsequently passed through the receiver they acquire the differential phase of the receiver. This reasoning is valid if the H and V fields are transmitted simultaneously, as done in the current implementation on the KOUN radar. In case of sequential transmission (of H and V components) the backscatter differential phase obtained from chaff is equal to the sum of the transmitted differential phase and differential phase of the receiver (i.e., total differential phase of the radar system). We speculate that very broad distribution of the differential phase in chaff is primarily due to high measurement errors attributed to very low cross-correlation coefficient (between 0.2 and 0.5). Similar analysis of differential phase in ground clutter reveals almost uniform distribution of  $\Phi_{DP}$  within the interval between  $0^\circ$  and  $180^\circ$ . The  $\rho_{hv}$  values from ground clutter are significantly higher than the corresponding values from chaff (Fig. 5), thus one expects smaller measurement errors of  $\Phi_{DP}$  in ground clutter. The observed uniform distribution of differential phase from ground clutter indicates that its intrinsic  $\Phi_{DP}$  (i.e., backscatter differential phase void of any measurement errors) might be uniformly distributed as opposed to chaff for which intrinsic differential phase upon scattering is likely zero.

Scattergrams of differential reflectivity and correlation coefficient vs reflectivity factor at SNRs  $> 10$  dB and from the region of chaff are displayed in Figs. 6 and 7. These data are from six scans at  $0.5^\circ$  elevation between the times 20 and 21 UTC. The average value of  $Z_{DR}$  is 3.36 dB without noise correction and 2.3 dB with correction; the average of  $\rho_{hv}$  it is 0.34 without noise correction and 0.36 with correction. For the noise corrected values the model (Fig. 1 and Fig. 2) suggests that the flutter angle is  $65^\circ$  (implied from  $Z_{DR}$ ) and  $75^\circ$  (implied from  $\rho_{hv}$ ). The agreement is reasonable considering that the model of uniform flutter angle distribution is a crude approximation of the true (but unknown) distribution and that clumping and flexing of chaff could be present. Still both polarimetric variables indicate that the needles have a large effective variation of flutter angles.

## 5. Conclusions

Two scattering models have been used to compute polarimetric variables of chaff. The models are Hertzian dipole and thin wire antenna. Pertinent polarimetric variables are differential reflectivity, correlation coefficient between copolar signals and linear depolarization ratio. Chaff is assumed to be uniformly distributed in azimuth. The angle between its axis and horizontal plane (flutter angle) is also uniformly distributed but between zero and a maximum value. It follows that the two models produce very similar results if the chaff length is half the radar wavelength or less. The linear depolarization ratio is uniquely related to the  $\rho_{hv}$  and  $Z_{dr}$  therefore these two variables are sufficient to separate chaff from precipitation echoes. Nonetheless, chaff could be confused with echoes from insects which produce similar values of  $\rho_{hv}$  and insects'  $Z_{dr}$  overlaps with the  $Z_{dr}$  of birds.

Chaff concentration can be computed from specific differential phase  $K_{DP}$  and volume reflectivity  $\eta$ . The values are little sensitive to the flutter angle hence it should be possible to estimate concentrations with less than 20% error. Thus chaff observation with a polarimetric radar offers attractive means for studying diffusion in the atmosphere.

One fortuitous observation of chaff demonstrated mighty separation of chaff from ground clutter and snow echoes. There is no overlap of the low correlation values (0.2 to 0.5) from chaff with those from ground clutter (0.6 to 0.8) or from snow (0.6 to 1). Low values from snow ( $<0.9$ ) are at low signal to noise ratios which occurs at distant ranges. Differential reflectivity of chaff is well separated from the one in snow, but in the absence of  $\rho_{hv}$  it can be mistaken to originate from rain.

#### *Acknowledgments*

We are grateful to R.J. Doviak for help concerning the antenna model and Chris Curtis for suggesting compact ways to numerically integrate two-dimensional integrals. Data presented here were collected during the Joint POLarization Experiment (JPOLE) which was organized by Terry Schuur and partly supported by the Office of System Technology of the National Weather Service. The NWS Radar Operations Center (ROC) contributed the basic RVP7 processor and display, which was subsequently enhanced to process dual polarization signals. John Carter and Valery Melnikov were responsible for the polarimetric aspects of the radar. Alan Siggia, from Sigmet, resolved numerous technical details needed to operate the RVP7 processor in dual polarization mode. Mike Schmidt and Richard Wahkinney made extensive modifications of microwave circuitry and controls. Allen Zahrai led the team of engineers who designed the new system which



enabled scanning strategies and allowed flexibility. Funding by the NWS Office of Science and Technology and the FAA over the last few years made this research possible.

## REFERENCES

Brandt M. B., and D. V. Atkin, 1998: Chaff in the vicinity of thunderstorms in Southern California on 6 June 1997. NWS, Western Region Technical Attachment No. 98-04 February 3, 1998.

Bringi, V.N. and V. Chandrasekar, 2001: Polarimetric Doppler Weather Radar, Principles and Applications. Cambridge University Press, Cambridge, UK, p. 636.

Brooks, E. M., J.D. Marwitz, and R.A. Kropfli, 1992: Radar Observations of transport and diffusion in clouds and precipitation using TRACIR. *J. Atmos. Oceanic Technol.* **9**, 226-241.

Doviak, R. J. and D. S. Zrnić, 1993: *Doppler Radar and Weather Observations*. 2nd Ed. Academic Press, Inc., 562 pp.

Evans, K.F., and J. Vivekanandan, 1990: Multiparameter radar and microwave radiative transfer modeling of nonspherical atmospheric ice particles. *IEEE Tr. Geoscience Remote Sens.* **28**, 423-437.

Hildebrand, P. H., 1977: A radar study of diffusion in the lower atmosphere. *J. Appl. Meteor.*, **16**, 493-510.

Holitz, F. J., and H. W. Kasemir, 1974: Accelerated decay of thunderstorm electric fields by chaff seeding. *J. Geophys. Res.*, **79**, 425-429.

Holt, A.R., and J.W. Shepherd, 1979: Electromagnetic scattering by dielectric spheroids in the forward and backward directions. *J. Phys. A Math. Gen.*, **12**, 159-166.

Jordan, E.C., and K.G. Balmain, 1968: Electromagnetic Waves and Radiating Systems. Prentice-Hall, Englewood Cliffs, p. 753.

Kasemir, H. W., F. J. Holitza, W. E. Cobb, and W. D. Rust, 1976: Lightning suppression by chaff seeding at the base of thunderstorms. *J. Geophys. Res.*, **81**, 1965–1970.

Kraus, J.D., 1950: Antennas, McGraw-Hill Inc. p. 553.

Maddox, R.A., Kenneth W. Howard, and Charles L. Dempsey, 1997: Intense Convective Storms with Little or No Lightning over Central Arizona: A Case of Inadvertent Weather, Modification? *J. Appl. Meteor.*, **36**, 302-314.

Martner B.E., J. D. Marwitz, and R.A. Kropfli, 1992: Radar observations of transport and diffusion in clouds and precipitation using TRACIR. *J. Atmos. Oceanic. Technol.* **9**, 226-242.

Ryzhkov, A.V., 2001: Interpretation of polarimetric radar covariance matrix for meteorological scatterers: Theoretical analysis. *J. Atmos. Oceanic. Technol.* **18**, 315-328.

Vasiloff, S, and M. Struthwolf, 1997: Chaff mixed with radar weather echoes, NWS, Western region technical attachment No. 97-02, January 17, 1997.

Ziegler, C. L., E. N. Rasmussen, T.R. Shepherd, A.I. Watson, and J.M. Straka, 2001: Evolution of low-level rotation in the 29 May 1994 Newcastle-Graham, Texas, storm complex during VORTEX. *Monthly Weather Review*, **129**, 1339-1368.

Zrnic, D. S., and A. Ryzhkov, 1999: Polarimetry for weather surveillance radar. *Bulletin of the American Meteorological Society*, **80**, 389-406.

## List of Figures

1. Differential reflectivity as a function of the wobbling angle, defined as the maximum (positive as well as negative) deviation of the chaff axis from the horizontal plane. The lengths of modeled chaff as a thin antenna model are indicated in terms of wavelength.
2. Cross correlation coefficient for the same models as in Fig. 1.
3. Linear depolarization ratios for a dipole and thin resonant chaff. Results for other smaller lengths are indistinguishable from the dipole model.
4. Ratio  $(K_{DP})^2/\eta$  for the thin wire model (lengths as fractions of wavelength are indicated) and the dipole model. The ordinate is in units of  $\lambda^2 N_o$ .
5. Fields of polarimetric variables from regions of ground clutter, chaff, and snow. Data were obtained during the Joint Polarization Experiment (JPOLE) on Feb 6, 2003 at 2100 UTC from a scan at 0.5 deg elevation.
6. Scattergram of the correlation coefficient vs reflectivity factor from chaff. Data were collected on Feb 6, 2003.
7. Scattergram of differential reflectivity vs reflectivity from chaff.

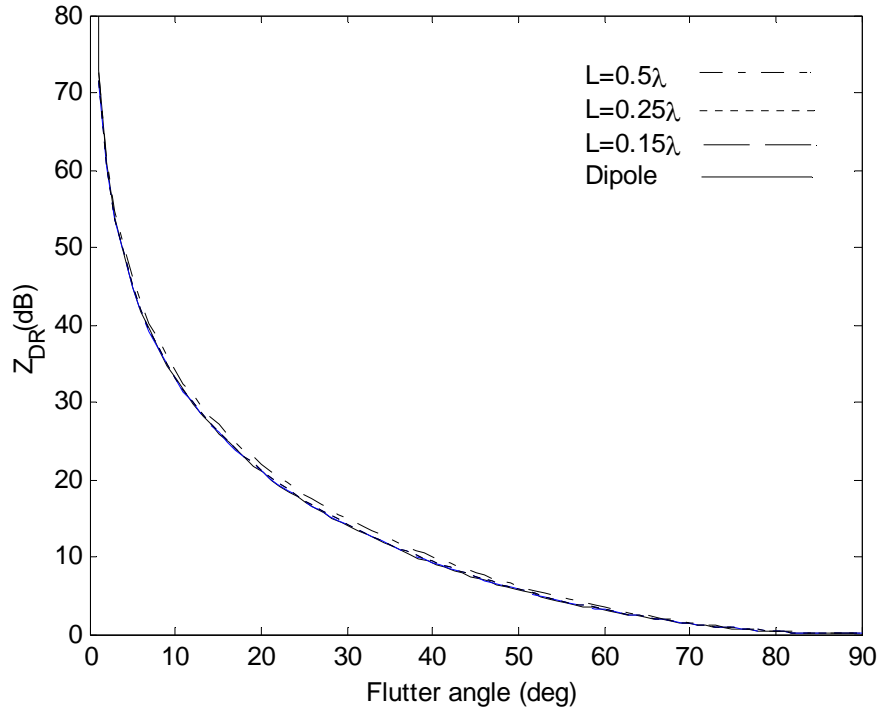


Fig. 1. Differential reflectivity as a function of the flutter angle, defined as the maximum (positive as well as negative) deviation of the chaff axis from the horizontal plane. The lengths of modeled chaff as a thin antenna model are indicated in terms of wavelength.

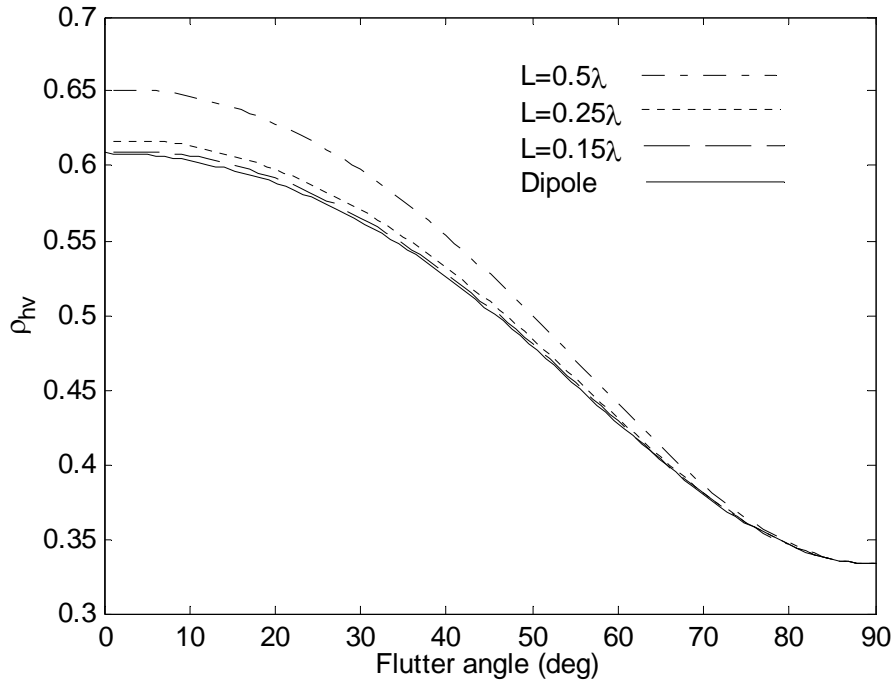


Fig. 2. Cross correlation coefficient for the same models as in Fig. 1.

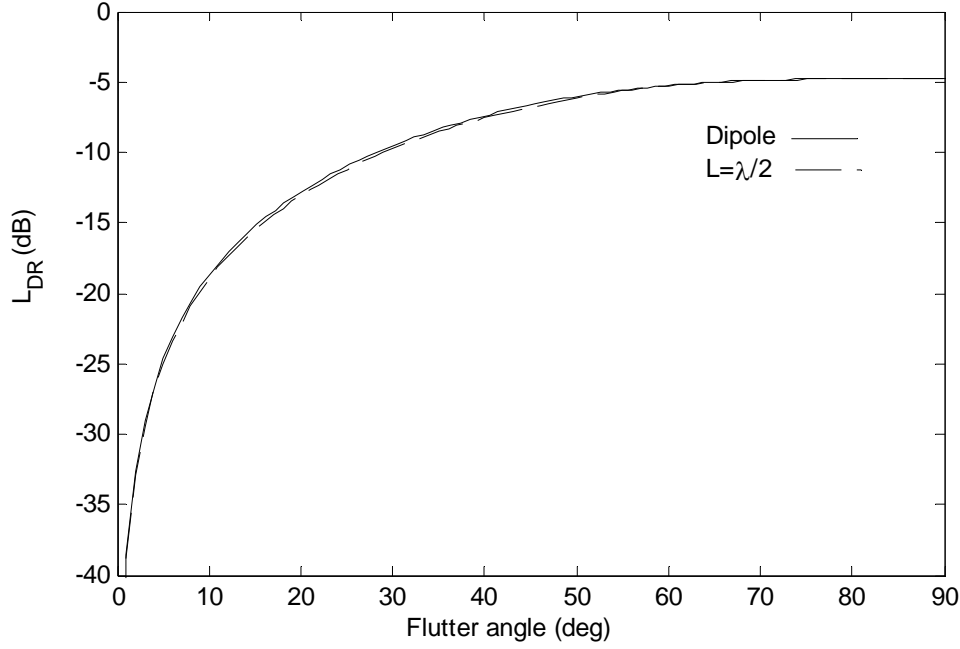


Fig. 3. Linear depolarization ratios for a dipole and thin resonant chaff. Results for other smaller lengths are indistinguishable from the dipole model.

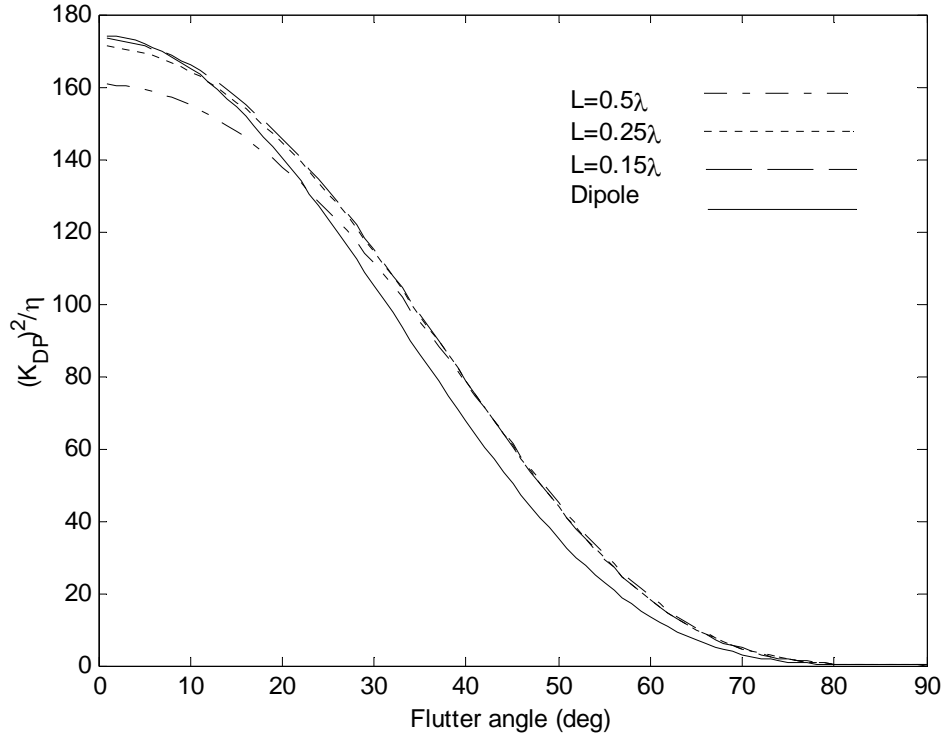


Fig. 4. Ratio  $(K_{DP})^2/\eta$  for the thin wire model (lengths as fractions of wavelength are indicated) and the dipole model. The ordinate is in units of  $\lambda^2 N_o$ .

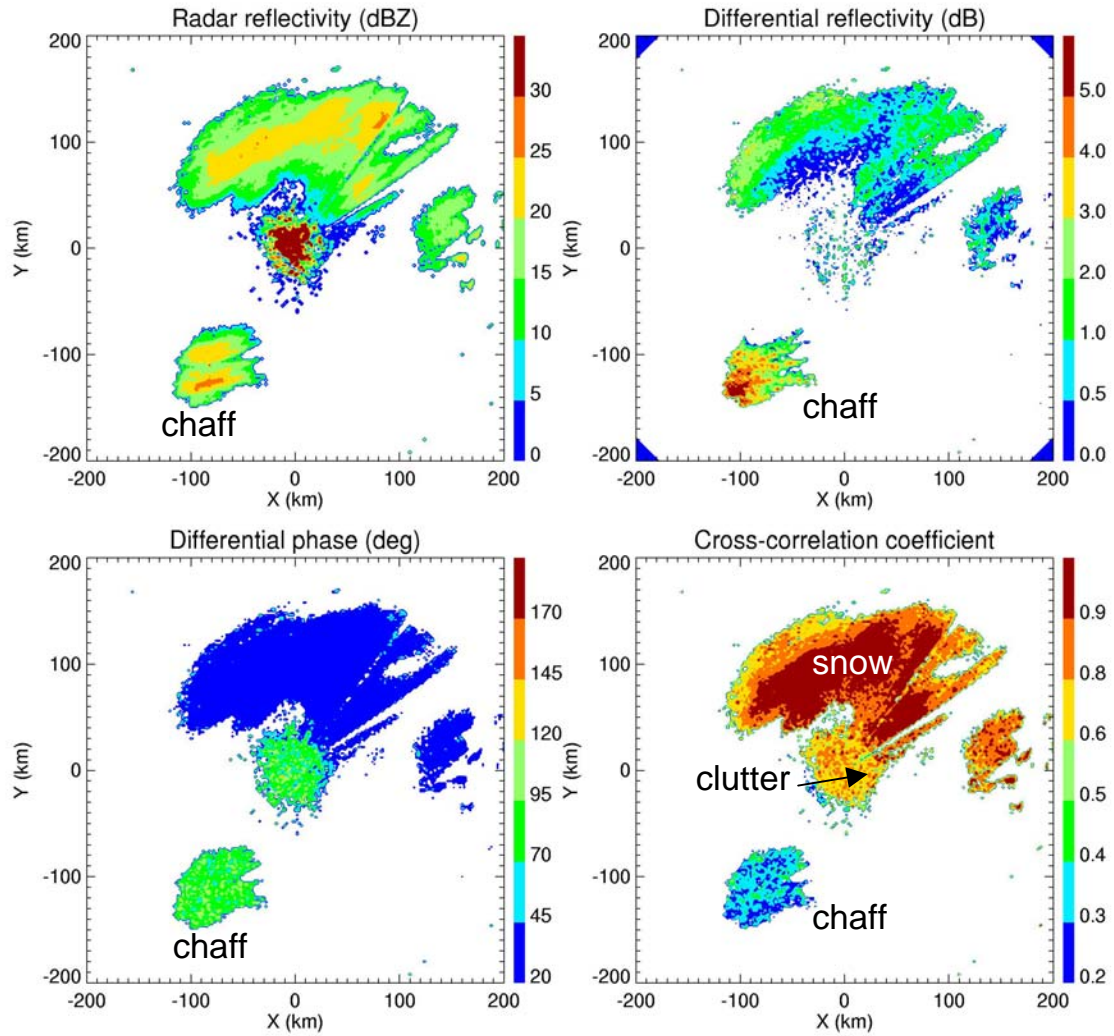


Fig. 5. Fields of polarimetric variables from regions of ground clutter, chaff, and snow. Data were obtained during the JPOLE experiment on Feb 6, 2003 at 2100 UTC from a scan at 0.5 deg elevation.

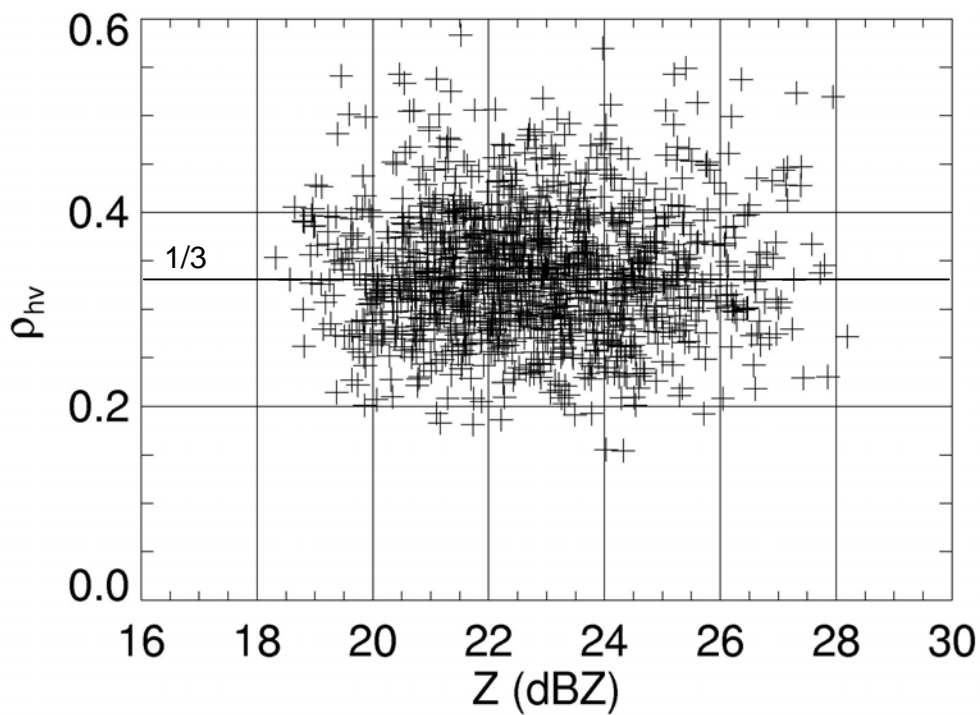


Fig. 6. Scattergram of the correlation coefficient vs reflectivity factor from chaff. Data were collected on Feb 6, 2003.

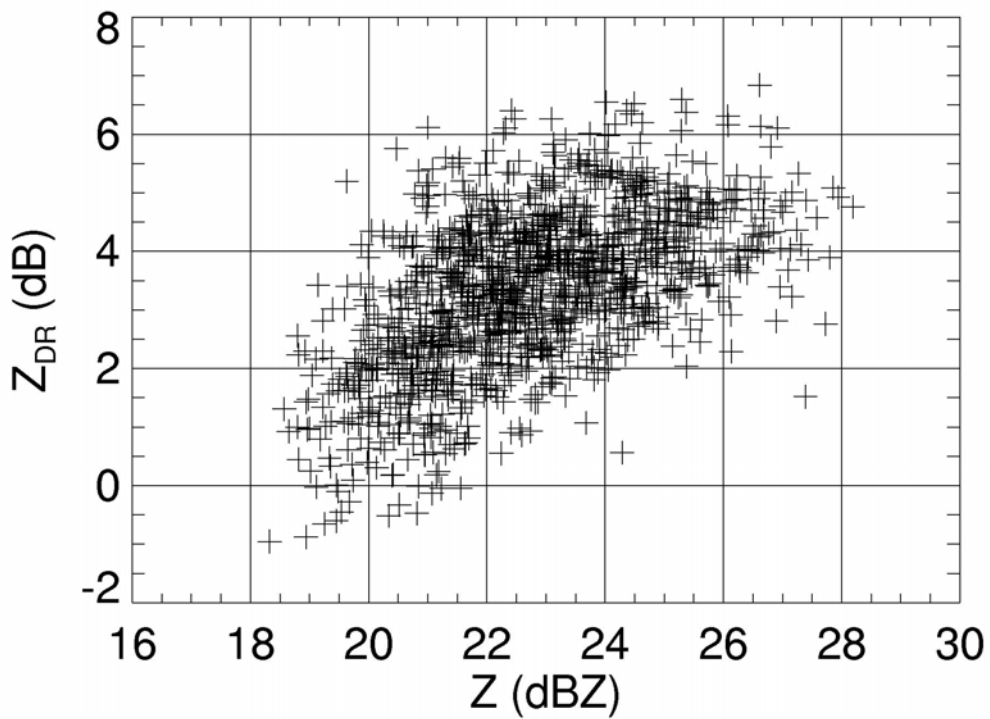


Fig. 7. Scattergram of differential reflectivity vs reflectivity from chaff.

S. E. Giangrande and A.V. Ryzhkov

Cooperative Institute for Mesoscale Meteorological Studies, University of Oklahoma

## 1. Introduction

A fuzzy logic approach has been adopted for operational polarimetric hydrometeor classification with the NSSL KOUN prototype polarimetric WSR-88D. This approach exhibits good performance for discrimination between meteorological and non-meteorological echoes, and improved detection of hail. Yet, the distinction between light rain and dry aggregated snow is challenging because of small polarimetric contrasts between these media. Therefore, identification of the melting layer is necessary to delineate liquid and frozen particles.

This paper examines a technique for melting layer detection with dual-polarization weather radars. Recent studies by Brandes and Ikeda (2004) focus on freezing level detection using polarimetric signatures. However, the transition from rain to snow occurs at the bottom of the melting layer, not at the 0°C isotherm. Thus, our goal is to estimate the location of the bottom of the melting layer. Establishing this height is important for accurate rainfall estimation and the detection of the regions with potential bright band contamination.

## 2. Description of the method

The technique for bright band detection takes a slightly different approach than the one suggested by Brandes and Ikeda (2004). Model profiles are not utilized. Since the linear depolarization ratio  $L_{DR}$  is unavailable with the KOUN radar, we make use of differential reflectivity  $Z_{DR}$ .

The major problem with polarimetric melting layer detection is that radar reflectivity  $Z$ ,  $Z_{DR}$ , and correlation coefficient  $\rho_{HV}$  bright band signatures do not coincide in height. Therefore, melting layer detection is determined by looking at  $Z$  and  $Z_{DR}$  maximums in the vicinity of  $\rho_{HV}$  dips. In general, polarimetric measurements of the melting layer are expected to fall within the range of 0.97 to 0.92 for  $\rho_{HV}$ , with maximum values between 29–47 dBZ for  $Z$  and  $Z_{DR}$  values greater than 0.8 dB.

Slant range dependencies of  $Z$  versus  $\rho_{HV}$ ,  $Z_{DR}$ , and differential phase  $F_{DP}$  at the 4.5° elevation angle (180° azimuth) are shown in Fig. 1(b,c,d) for an event on 4 June 2003 (1330Z). A pronounced drop in  $\rho_{HV}$  to values below 0.97 begins at slant range = 30 km (approx. 2.2 km above the radar) followed by relative maximums in  $Z_{DR}$ ,  $Z$ , and  $F_{DP}$  in the subsequent 5–10 km slant range interval. Notable is the return of  $\rho_{HV}$  to higher values

above the melting layer, which accompanies stable  $Z_{DR}$  values near 0.3 dB consistent with the presence of dry aggregated snow.

The results of bright band identification are provided in Fig. 1a. The approach incorporates range-gate data from 5 KOUN elevation angles between 4.5° and 8.7° and all available azimuths. Heights represent the mean radar beam height of range-gates that register as a signature. The results indicate modest azimuthal variability in the height of initial melting layer interaction. Highest initial signatures occur at heights (approx. 2.6 km) located in the direction of the warmest surface temperatures (south and west). Interaction with the melting layer in northerly directions occurs as low as 2.2 km. The depth of the melting layer signature also varies significantly with azimuth. The vertical extent of these signatures is greatest in the direction of the warmest surface temperatures, and generally varies between 0.6 – 1.2 km.

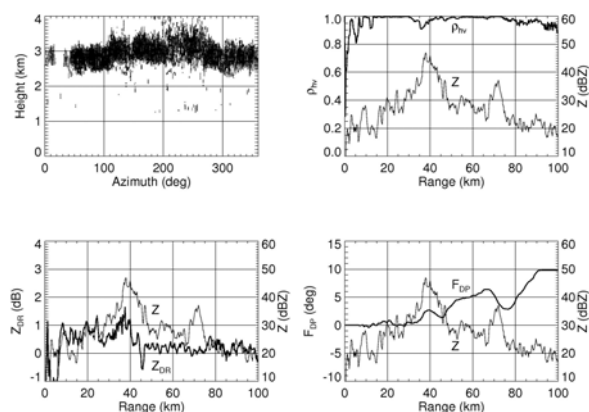


Fig. 1. (a) Results of polarimetric bright band detection for June 4, 2003 (1330Z). Slant range dependencies of (b)  $\rho_{HV}$ , (c)  $Z_{DR}$ , and (d)  $F_{DP}$  for the 180° azimuth at 4.5° are also displayed.

It is possible that no pronounced melting layer signature exists. As opposed to previous versions of the hydrometeor classification algorithm, data for melting layer detection can be ingested from several elevation angles to maximize available signatures. Model output may be ingested as quality control for bright band location or to supplement the hydrometeor classification until sufficient radar statistics can be accumulated. Studies performed during the Joint Polarization



Experiment (JPOLE) suggest that the optimal elevations for melting layer detection are between 4° and 9°.

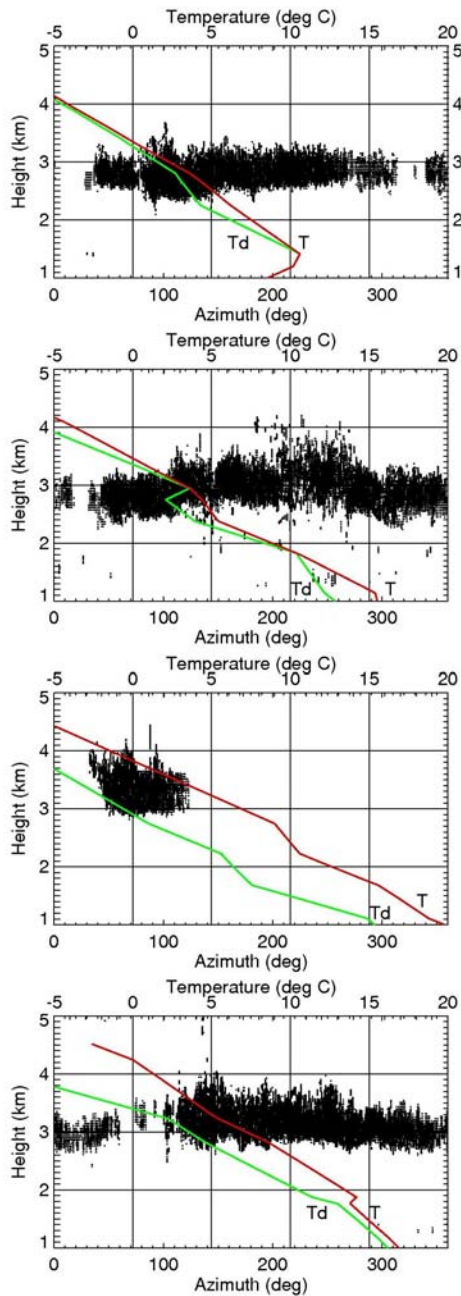


Fig. 2. Results of bright band detection for 4 warm season events during 2003 on (a) May 21, (b) June 4, (c) June 11, and (d) June 26. Temperature (red lines) and dewpoint (green lines) data from soundings launched near KOUN are overlaid on the plots.

### 3. Estimation of the bright band height and thickness for the warm season rain events

Polarimetric bright band detections for 4 warm season events in 2003 (May 21, June 4, June 11, and June 26) are shown in Fig. 2. Each image represents a bright band detection obtained using a single radar volume for each event (volume starting from 1309Z, 1330Z, 0510Z, and 1720Z, respectively). Prominent melting layer signatures were frequently associated with convective warm season storms (more often than anticipated) during the JPOLE campaign. Optimum signatures were linked to trailing stratiform regions behind squall lines and anvil regions of thunderstorms. Partial sounding information for temperature and dewpoint from soundings launched near KOUN has been provided for each event from the closest available time (either 00Z or 12Z).

Sounding information in Fig. 2 generally agrees with the estimated location of melting layer signatures obtained using KOUN. Polarimetric signatures of the melting layer begin at or below the height of 2.5 km for several events. Temperatures corresponding to the layer of pronounced polarimetric bright band signatures typically fall between 2°C–8°C, slightly warmer than observations of several studies (e.g., Mitre et al. (1990, Brandes and Ikeda (2004)) for the later events. The slight discrepancy between sounding temperatures and previous observations may be attributed to several factors. First, the assumption of mean beam height causes a slight underestimation in height detection. In addition, the available environmental soundings do not completely represent the in-cloud temperature profile for these events. A temporal mismatch may pose an issue for accurate comparisons if the environment is significantly altered by the precipitation regime. It is evident from the top two events in Fig. 2 that results obtained for bright band detection displayed optimum agreement with previous observational studies when soundings in close temporal and spatial proximity to the radar measurements were utilized.

Surprisingly, potential bright band contamination of radar variables for several of these events begins at slant ranges within 140 km of the KOUN radar, a significant consideration for the warm season. This finding has immediate implications for data quality, as well as for defining the limits of accurate rainfall estimation. The azimuthal variability of the height and depth of melting layer signatures is also significant for these events. Relative differences in detected heights translate into several tens of kilometers in horizontal coverage. Most variability can be attributed to larger-scale temperature field. Localized variability may be related to the location of downdrafts in convective cells.

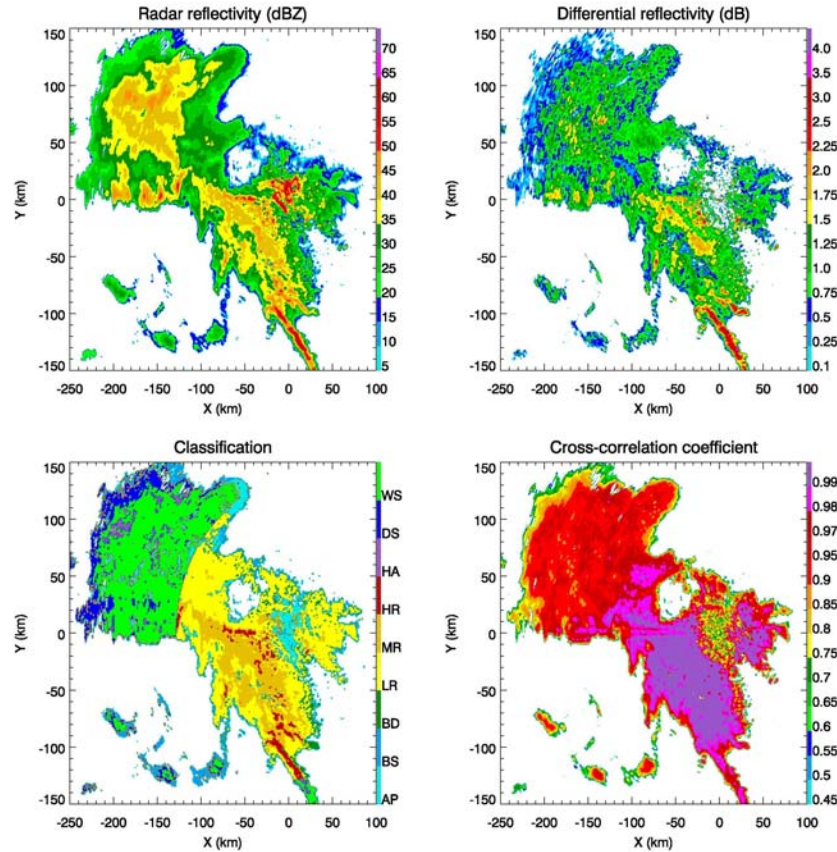


Fig. 3. Composite plot of polarimetric variables and the results of hydrometeor classification at the 0.5° elevation for the event on June 4, 2003 (1330Z)

#### 4. Polarimetric hydrometeor classification and its implications for radar rainfall estimation

The 4 June 2003 storm (Fig. 1, Fig 2b, and Figs. 3-5) provides an excellent illustration of warm season bright band signatures and the implications of melting layer contamination for hydrometeor classification, data quality, and rainfall estimation. The event can best be described as a widespread region of moderate precipitation with several embedded convective elements.

Fig. 3 shows several PPI images from the 0.5° elevation angle at 1330Z. It is difficult to associate the NW part of echo with the bright band contamination provided only Z is used.  $\rho_{HV}$  provides the best indication of melting layer contamination for this elevation angle. In contrast, consider the PPI images at the 4.5° elevation angle shown in Fig. 4 from the same radar volume. The bright band signature for all variables is now clear. Notable is the dramatic lowering of  $Z_{DR}$  measurements

above the melting layer associated with the presence of dry aggregated snow.

Hydrometeor classification results have been included with each series of PPI images. Areas associated with mixed phase hydrometeors (those matching bright band criteria) have been assigned a wet snow 'WS' classification. Additional classification is performed for light rain 'LR', moderate rain 'MR', heavy rain 'HR', hail 'HA', dry snow 'DS', big drops 'BD', and two non-meteorological classes, 'AP' and biological scatterers 'BS'.

Radar rainfall accumulation for the hour between 1300-1400Z is shown in Fig. 5. The results of hydrometeor classification have been utilized to remove non-meteorological contaminants from the accumulations. Radar rainfall estimates include a conventional  $R(Z)$  algorithm and a polarimetric  $R(Z, K_{DP}, Z_{DR})$  algorithm described in Ryzhkov et al. (2003). Oklahoma Mesonet gauge accumulations have been overlaid on the rainfall plots for comparison. Errors in the conventional  $R(Z)$  estimates associated with the

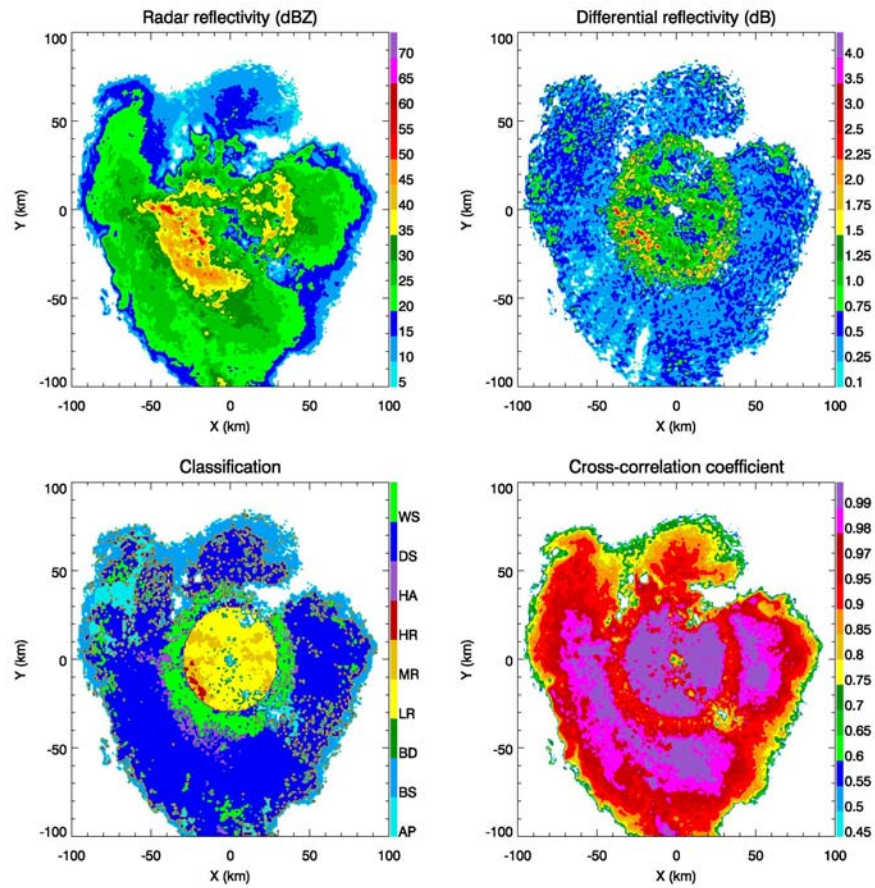


Fig. 4. Same as Fig. 3, but for the 4.5° elevation.

location of intense convective cells and bright band contamination are especially pronounced. Polarimetric estimates outperform the conventional estimate for all regions, however the most substantial improvements are witnessed in the regions with an absence of melting layer contaminants.

## Conclusions

## References

Brandes and Ikeda  
Ryzhkov et al  
Scharf





#### **04.6.14 Multi-Radar Composites**

---

**Objective: Examine aspects of multiple radar integration and algorithms.**

##### **04.6.14.1 3-D mosaic survey to the AWRP Product Development Teams**

(This task was completed in the 1st Quarter.)

##### **04.6.14.2 Enhance the 3D mosaic based on strategies proposed in task 04.6.14.1.**

A survey was conducted to receive feedback on enhancements required for the 3D mosaic and derivative products. Based on the PDT feedback, two areas of enhancements are proposed: 1) data quality control and 2) gap-filling below the lowest tilt. The 1<sup>st</sup> item is addressed in task 04.6.14.9 (see below). The 2<sup>nd</sup> item will be addressed in the following steps:

- i) Year 2004 – to generate a lowest (in terms of altitude) radar-observable reflectivity field (called “hybrid scan reflectivity” or HSR hereafter). The HSR is a 2D product derived from the 3D reflectivity mosaic grid by searching each grid column from bottom to top and obtaining the very first valid reflectivity value. The height (HSRH, in meters above ground level) associated with the HSR field will also be computed using high-resolution digital elevation map (DEM). The HSR and HSRH fields will provide information about the radar observations closest to the earth surface.
- ii) Year 2005 – to develop and test various methodologies for computing vertical profiles of reflectivity (VPR) from base level reflectivity data and use the VPR to extrapolate radar reflectivity to the surface.
- iii) Year 2006 and beyond – to incorporate TDWR (Terminal Doppler Weather Radar) and CASA (Collaborative Adaptive Sensing of the Atmosphere) radars into the 3D mosaic and in the 4D dynamic grid as proposed in the Advanced Weather Radar Technologies PDT’s 7-year plan for year 2005 – year 2011.

##### **04.6.14.3 Generate and disseminate 3D mosaic gridded data as requested by PDTs.**

The activities for this quarter include continued support of real-time CIWS 3D grid data to other PDTs.

##### **04.6.14.4 Maintenance and regular updates of the real-time 3-D mosaic in the CIWS region.**

The activities for this quarter include two software updates to the 3-D mosaic algorithm. A minor update was made in the pre-process code of the 3D mosaic for ingesting a new Level-II data format implemented in the WSR-88Ds (Build 5) by the National Weather Service (NWS). A major update was implemented for the new scan strategies or VCPs (see Table 1) also part of

the WSR-88Ds (Build 5). New hybrid scan reference files were generated to encompass the new VCP 12 (Table 1).

The legacy 4-tilt hybrid scans\* were tilt number-referenced. A tilt-number referenced hybrid scan is a 2D polar grid (e.g., 1°×1 km) of tilt numbers that represent the lowest radar beams that satisfy the following criteria:

- 1) Bottoms of the beams clear the ground by at least 50 m (adaptable parameter).
- 2) Radar power blockages in the beams are less than 60% (adaptable parameter).

The radar power blockages are calculated using pre-defined elevation angles assuming normal propagations of radar beam. In the reflectivity quality control scheme, all echoes below the hybrid scan are assumed to be contaminated by the ground and are removed. Previously each radar has only one hybrid scan since the old VCPs (11, 21, 31, 32) contain approximately the same elevation angles in the lowest four tilts. Since March 2004, two new VCPs have been implemented in the WSR-88Ds (Table 1). The new VCP 121 has the same set of elevation angle as in VCP 21, while VCP 12, has different elevation angles in the lowest four tilts (Table 1). Hence, the legacy tilt number-based hybrid scans cannot be used for the new VCP 12.

\*O'Bannon, 1997: Using a 'terrain-based' hybrid scan to improve WSR-88D precipitation estimates. *Preprints, The 28th International Conference on Radar Meteorology*, September 7-12, 1997, 506-507

**Table 1 Elevation angles (°) in operational VCPs for WSR-88Ds. The two new VCPs (12 and 121) are in bold font.**

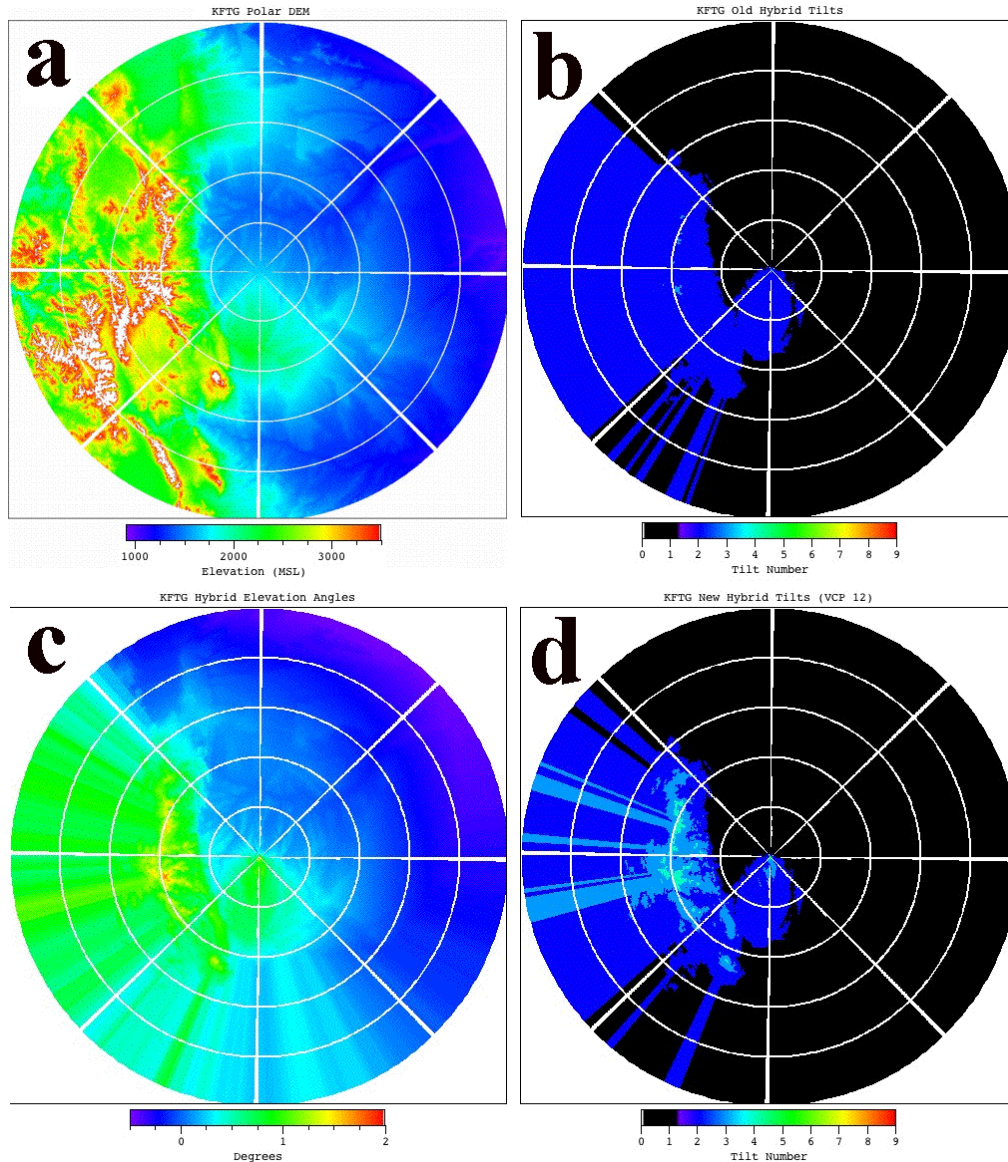
Tilt #	1	2	3	4	5	6	7	8	9	10	11	12	13	14
VCP 11	0.5	1.45	2.4	3.35	4.3	5.2	6.2	7.5	8.7	10.0	12.0	14.0	16.7	19.5
VCP 21	0.5	1.45	2.4	3.35	4.3	6.0	9.9	14.6	19.5					
VCP 31	0.5	1.5	2.5	3.5	4.5									
VCP 32	0.5	1.5	2.5	3.5	4.5									
<b>VCP 12</b>	<b>0.5</b>	<b>0.9</b>	<b>1.3</b>	<b>1.8</b>	<b>2.4</b>	<b>3.1</b>	<b>4.0</b>	<b>5.1</b>	<b>6.4</b>	<b>8.0</b>	<b>10.0</b>	<b>12.5</b>	<b>15.6</b>	<b>19.5</b>
<b>VCP121</b>	<b>0.5</b>	<b>1.45</b>	<b>2.4</b>	<b>3.35</b>	<b>4.3</b>	<b>6.0</b>	<b>9.9</b>	<b>14.6</b>	<b>19.5</b>					

To account for VCP 12 and any future scan strategies, a new elevation angle-referenced hybrid scan was developed. The new hybrid scan consists of elevation angles on a regular 2D polar grid. The elevation angles are found through an iterative scheme and are the lowest radar beams that satisfy the same criteria as in the legacy hybrid scans. Detailed description of the new hybrid scan algorithm will be presented at the 11<sup>th</sup> Conference on Aviation, Range, and Aerospace Meteorology (4-8 October 2004, Hyannis, MA).

It is noteworthy that the elevation angle-referenced hybrid scan is independent of radar scan strategies. Therefore the new hybrid scan algorithm can be used for other type of radars such as TDWR or CASA.

In the quality control, the actual elevation angles of data are compared with the hybrid scan elevation angles and all echoes below the hybrid scan are removed.

Figure 1 shows an example of the old and new hybrid scans for the KFTG (Denver, CO) radar. Panel (a) shows the high-resolution terrain used for deriving the KFTG hybrid scans. Panel (b) shows the old tilt number-referenced hybrid scans for VCP 11, 21, 31 and 32. The tilt numbers were obtained by assuming the lowest four elevation angles are 0.5, 1.45, 2.4, and 3.35°. The new elevation angle hybrid scan is shown in panel (c), and the equivalent tilt number-referenced hybrid scans for VCP 12 is shown in panels (d).



**Figure 1** Topography and hybrid scan images for KFTG (Denver, CO) radar. Panel (a) shows the topography (m above MSL) within 250km range of KFTG site. Panel (b) shows the old tilt number-based hybrid scan. Panel (c) shows the new elevation angle (degrees) –based hybrid scan. Panel (d) shows an equivalent tilt number-based hybrid scan for new VCP 12.

**04.6.14.5 Develop computational strategies and run time scripts for the creation of a national (CONUS) 3-D mosaic using base level WSR-88D and TDWR data. Start 1 Oct 2003.**

(This task was completed in the first quarter for WSR-88Ds. The TDWR data were not available for integration in the real-time CONUS mosaic.)

**04.6.14.6 Prepare reference files and background data sets for a national mosaic. Start 1 Dec 2003.**

Reference files (3D mosaic lookup tables) have been generated for the all WSR-88D VCPs include the new VCP12 and VCP121. The ingest code for background and reference data sets including satellite and RUC model fields has been developed and implemented. Real-time satellite and RUC data are currently being ingested at NSSL. This task was completed during the 2<sup>nd</sup> quarter (31 Mar. 2004).

**04.6.14.7 Develop and prototype a real time system for the creation of national 3-D reflectivity mosaics for 14 tiles encompassing the CONUS. Start 1 Mar 2004.**

An experimental real-time nation 3D reflectivity mosaic system has been implemented and running since 1 May 2004. The 3D reflectivity mosaic system is a major component of NSSL's National Mosaic and multi-sensor QPE (NMQ) system and test bed. An overview flowchart of the NSSL NMQ 3D radar mosaic system is shown in Figure 2.

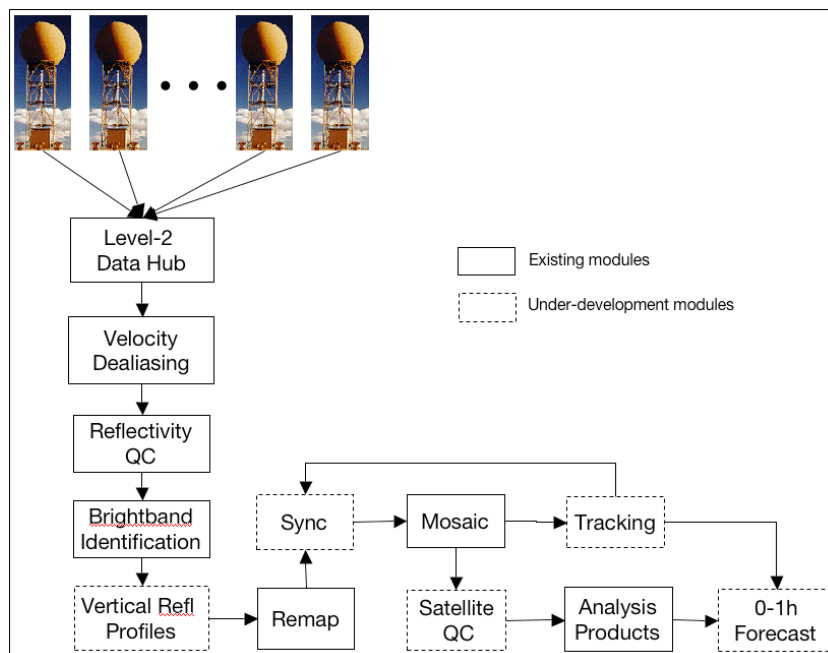


Figure 2 An overview flowchart of the NMQ 3D mosaic system.



Since March 2004, base level (or “level-2”) data from 130+ WSR-88D radars are being sent to the University of Oklahoma (OU) -- one of three NWS level-2 data hubs – utilizing the Local Data Management (LDM, <http://my.unidata.ucar.edu/content/software/ldm/index.html>) compression and across the Internet 2. The use of the LDM compression technique and the Internet 2 communications backbone has assured a very reasonable latency (mostly less than 1 minute) between when data are collected at the radar site and when the data are received by the NSSL NMQ system. The NMQ system receives the level-2 data directly from the OU radar hub. Once a volume scan of data from a radar has been fully received, the data are pre-processed for radial alignment, velocity dealiasing, reflectivity quality control, and brightband identification (Fig. 2). All these processes are performed in the native radar (spherical) coordinates. After the quality control, single radar reflectivity data are remapped from their native spherical to a Cartesian coordinate system. Once remapped, the individual radar data are mosaiced for individual geographical tiles across the CONUS. For computational efficiency in addition to utilizing an economic cluster computing architecture, the CONUS domain was divided into 14 regional tiles (Fig. 3) in which multiple radars are mosaiced. The sizes of individual tiles are determined by precipitation climatology (Fig. 4, [http://www.cpc.ncep.noaa.gov/research\\_papers/ncep\\_cpc\\_atlas/7/atlas\\_7.html](http://www.cpc.ncep.noaa.gov/research_papers/ncep_cpc_atlas/7/atlas_7.html)) and the radar sites distribution. Smaller tiles are associated with high frequency of precipitation and dense radar distributions and vice versa. The NMQ tiles are in the cylindrical equidistant map projection. Each tile consists of a 3D Cartesian grid with a horizontal resolution of  $0.01^\circ$  (longitude)  $\times$   $0.01^\circ$  (latitude) over 21 height levels ranging from 1 km to 17 km above mean sea level (MSL). The vertical grid interval is 500 m below 5 km MSL and is 1000 m above it. A stitching program has been developed to combine all the tiles together and to create a single final CONUS grid of reflectivity and derivative products.

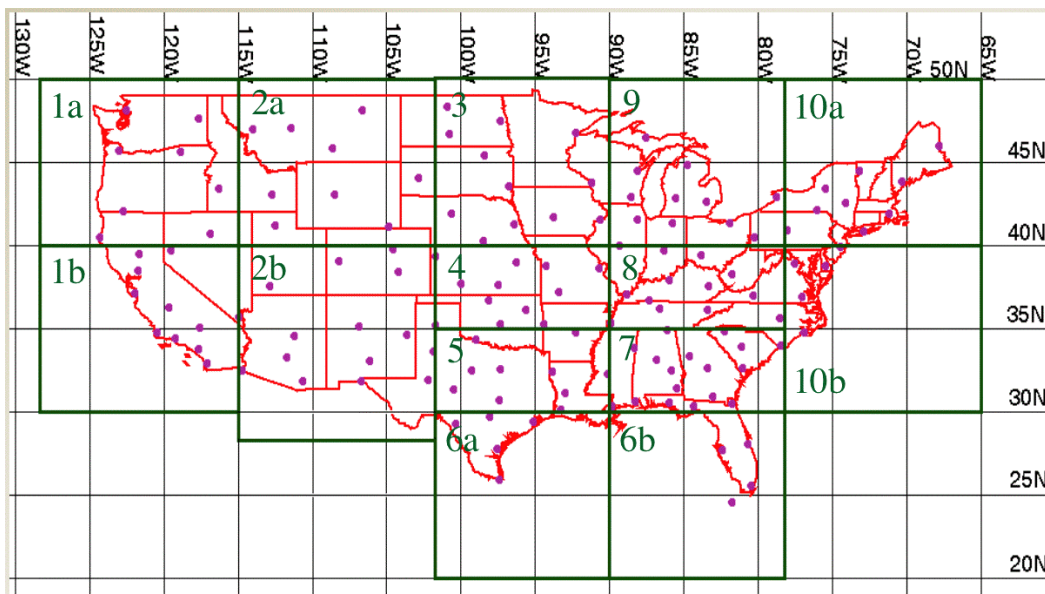


Figure 3 Geographical tiles that consist of the CONUS mosaic grid.

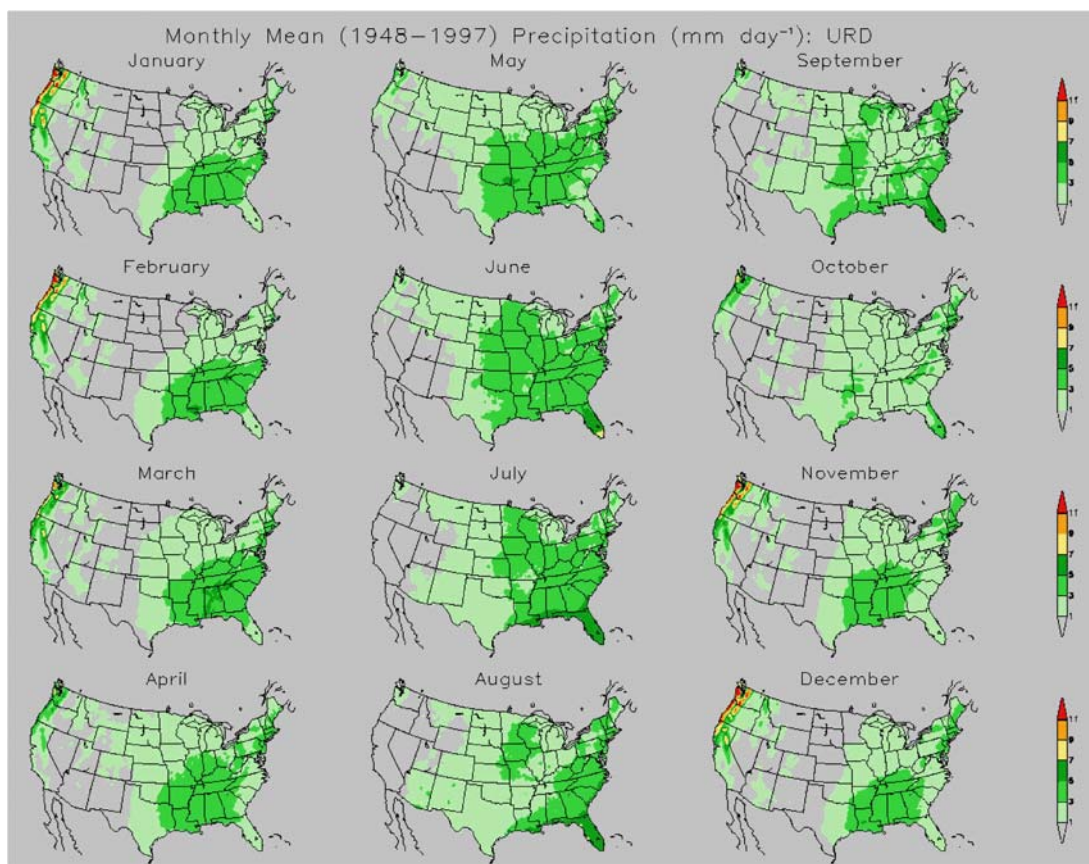


Figure 4 Monthly precipitation climatology over the CONUS domain.

The NMQ computer cluster architecture uses a Linux operating system and consists of 10 nodes with 2 CPU processors per node. Each CPU processor is 3.2GHz in speed and has 3GB RAM. Among the 10 computer nodes, 4 are used for single radar ingesting and pre-processing and 6 are used for spherical to Cartesian remapping and mosaicing. The network chart of the NMQ system is shown in Figure 5.

The performance of the NMQ 3D mosaic system has been closely monitored. A NMQ system monitoring web page (<http://nmqserver.protect.nssl/~qpeverif/>) has been instituted and performance statistics are displayed within the web page. The statistics include latencies of each process, radar data networking status, percentage of echo coverage, etc.

Figure 6 shows an interface for monitoring the status of single radar ingesting and pre-processing. When users click on the individual radar circles, plots of performance statistics for single radar processes will appear (Fig. 7). The plots include time series of 1) radar VCPs (panel a, Fig. 7), 2) latency of level-2 data over the network (from a radar site to the NSSL NMQ system (panel b, Fig. 7), 3) total clock time for running single radar processes (i.e., alignment, reflectivity QC, velocity dealiasing, etc, panel c, Fig. 7), and 4) percentage area with -30dBZ or higher echoes in the 460 km radar umbrella (panel d, Fig.7).

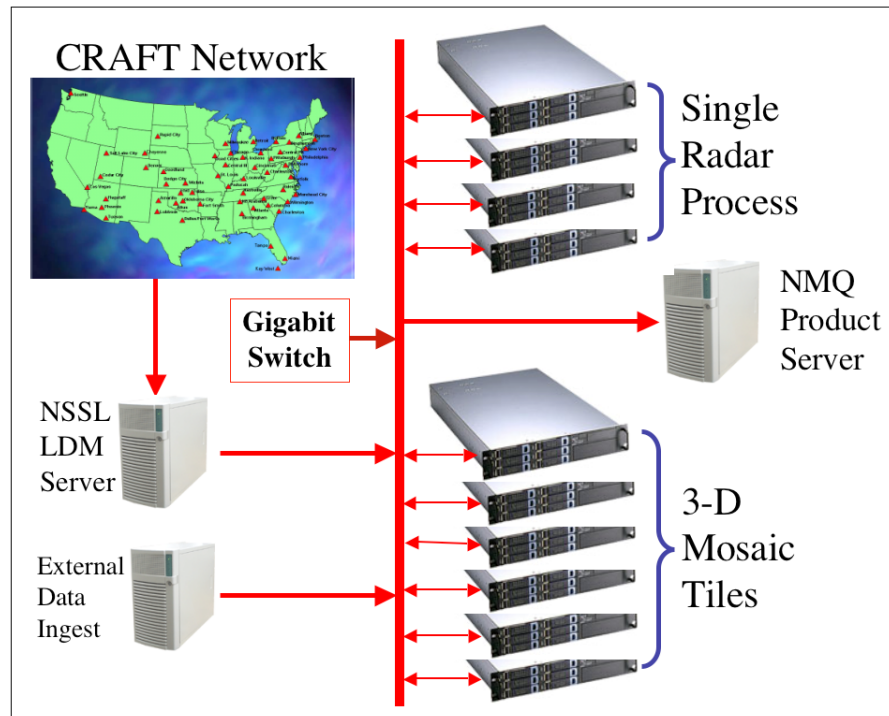


Figure 5 Illustration of the network infrastructure for the NMQ 3D mosaic system.

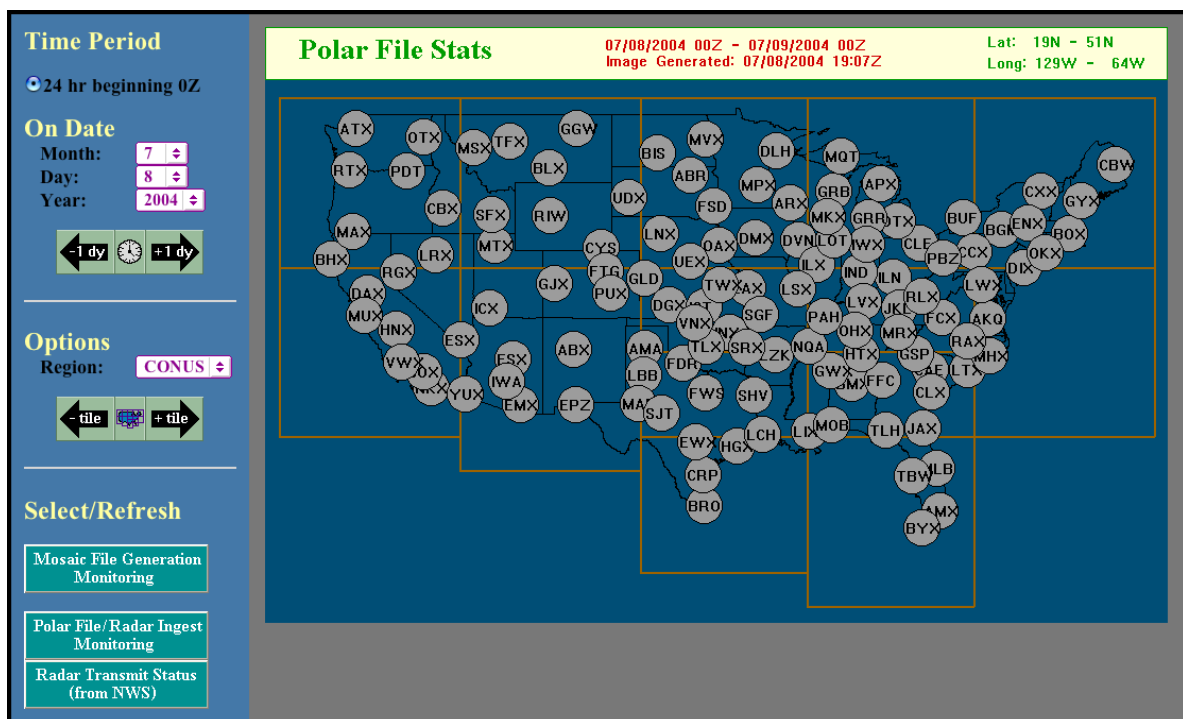


Figure 6 The interface for performance statistics of the single radar processes. When clicking on any one radars circle, plots of performance statistics will appear (Fig. 7).



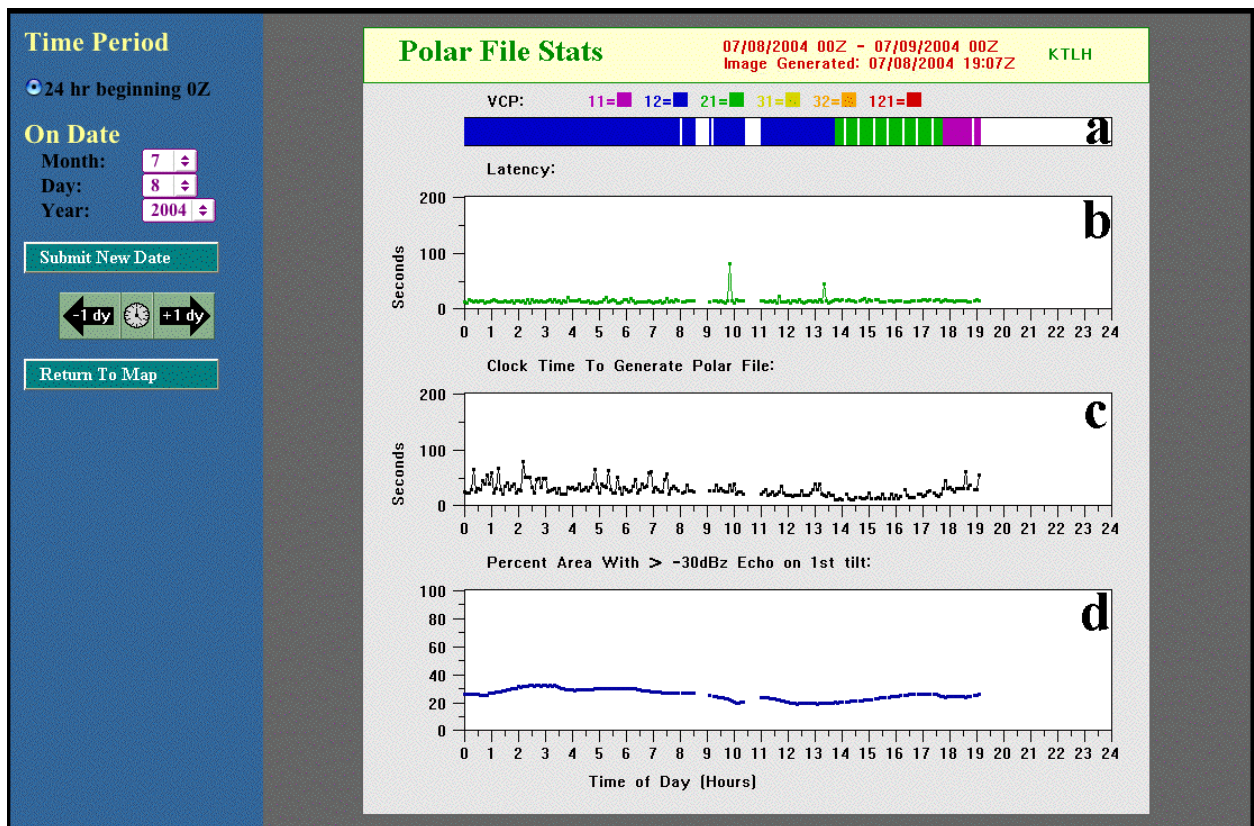


Figure 7 Example plots of performance statistics for a single radar processing. The plots show time series of (a) radar VCPs, (b) latency of level-2 data networking between the radar site and the NMQ system, (c) total clock time for running all single radar processes (i.e., alignment, reflectivity QC, velocity dealiasing, etc), and (d) the percentage area with  $-30\text{dBZ}$  or higher echoes in the 460 km radar umbrella. Two small data gaps are apparent around 08:45 and 10:45 UTC.

Figure 8 shows an interface for monitoring multiple-radar mosaic process. This page contains information about performance of the mosaic algorithm for each tile. The information includes the average and maximum clock times (in seconds) required by the mosaic process, number of radars that were used in each mosaic, number of product files being generated, etc. Note that the ideal number of radars for each tile was determined using all 156 NEXRAD sites. Currently only about 130 of the sites are sending level-2 data to the CRAFT hubs in real-time.

When a user clicks on individual the tiles (or choose an individual tile from the menu on the left side of the page), plots of performance statistics for the 3D mosaic process in the tile appear (Fig. 9). The plots include time series of 1) clock and CPU times for each mosaic run (panel a, Fig. 9), 2) number of radars went into the mosaic run (panel b, Fig. 9), and 3) percentage area with  $-30\text{dBZ}$  or higher echoes in the tile (panel c, Fig. 9). The example plots shown in Fig. 9 are for tile 7 (see Fig. 2) on 8 July 2004. An example composite reflectivity image at 19UTC for tile 7 is shown in Fig. 10.

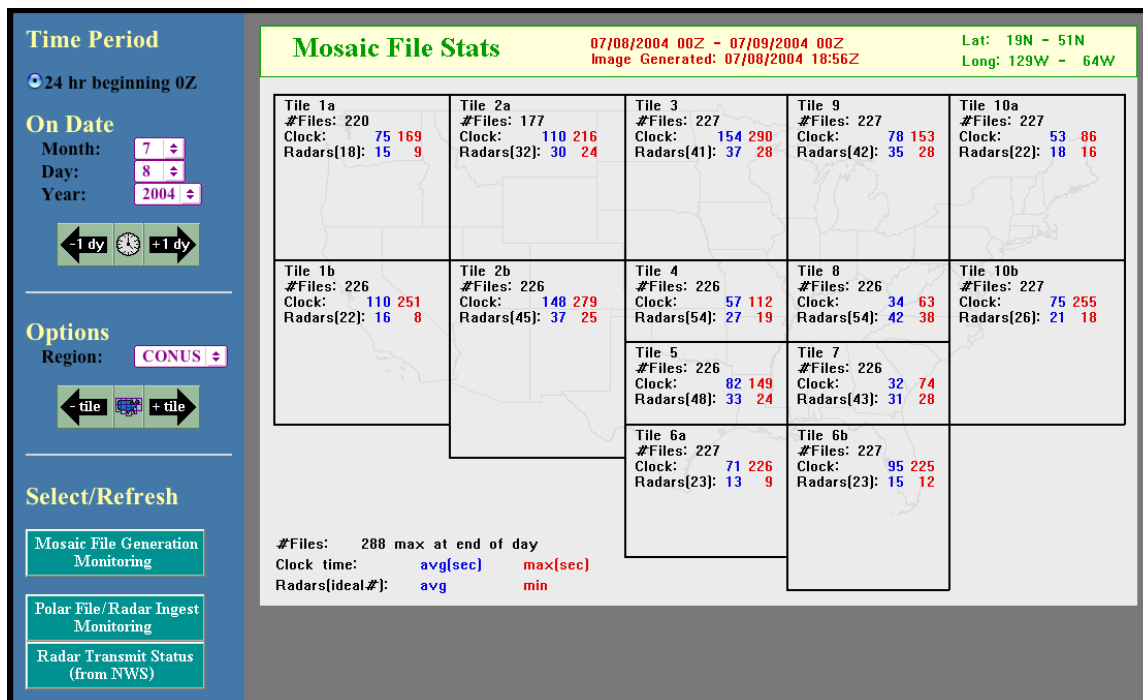


Figure 8

The interface for monitoring of the 3D mosaic process. When users click on any one of the tiles or choose a tile from the menu on the left of the page, plots of performance statistics of the mosaic algorithm in the tile will appear (Fig. 9).

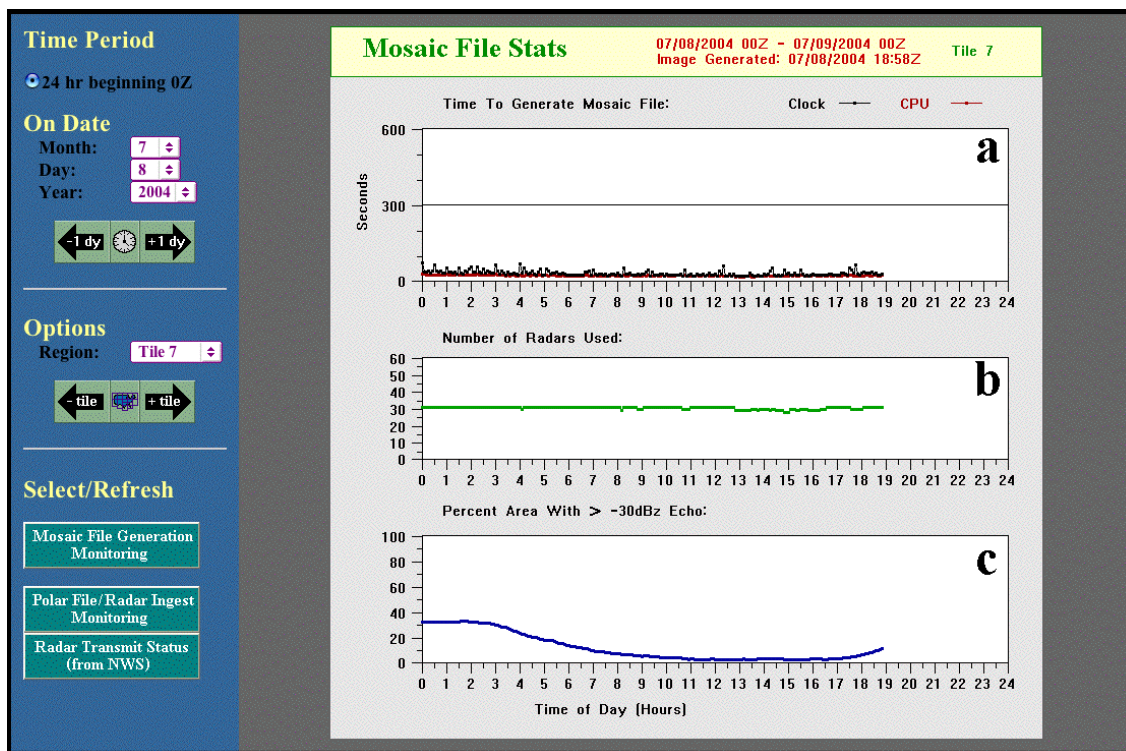


Figure 9 Example plots of performance statistics for the 3D mosaic process in tile 7. The statistics include time series of (a) clock and CPU times for running the 3D mosaic for the tile, (b) number of radars went



into the mosaic, and (c) the percentage area with -30dBZ or higher echoes in the tile. Note that the mosaic runs every 5 minutes.

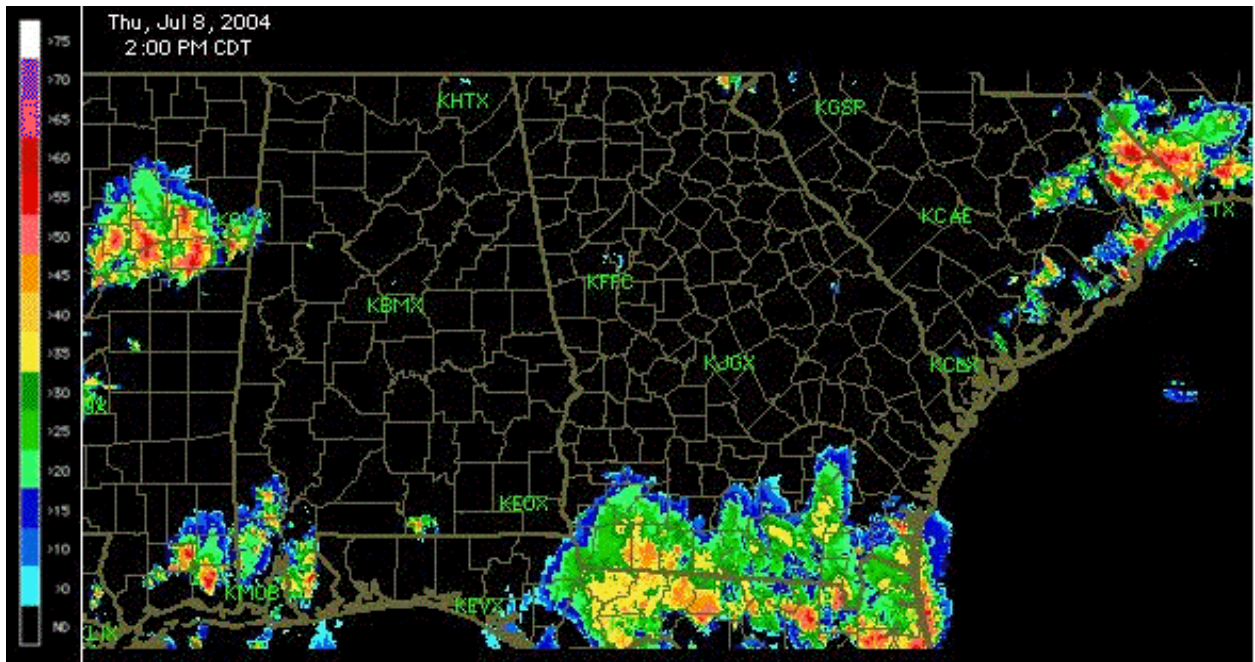


Figure 10 Example composite reflectivity image for tile 7 at 1900UTC on 8 July 2004.

The NMQ 3D mosaic system has been very stable during the testing period. Utilizing only 6 nodes, the NMQ can produce the 1-km resolution national 3D mosaic every 5 minutes more than 90% of the time. This indicates that the latency of the mosaic products from the end of data collections at radar sites is less than 15 minutes more than 90% of the time. The potential latency can be further reduced with additional computation resources or nodes.

Several hardware failures and problems were experienced during the initial implementation of the NMQ 3D mosaic system. The hardware failures and problems resulted in delaying the delivery of the 3D mosaic grid from 1 May to 30 June 2004 (Deliverable 04.6.14.E8). Most of the problems were resolved by 30 June 2004 and the cluster has been relatively stable since then. The NSSL is closely monitoring the hardware and working with the manufacture to minimize any potential hardware problems in the future.

#### **04.6.14.8 Prepare and implement NetCDF national 3-D mosaic data sets to PDT partners at NCAR and FSL. Start 1 Apr 2004.**

The CONUS 3D reflectivity mosaic grid has been generated since 30 June 2004 using ~130 radars level-2 data in real-time. An example composite reflectivity image for the CONUS domain is shown in Fig. 11a. Two zooming-in images for smaller regions are shown in Figs. 11a and 11b, respectively. The NMQ 3D mosaic grid data are produced and outputted using a NetCDF format. An online data archive is maintained for 7 days and then aged off to DVDs for

permanent storage. An anonymous ftp account has been established for users to retrieve the online data.

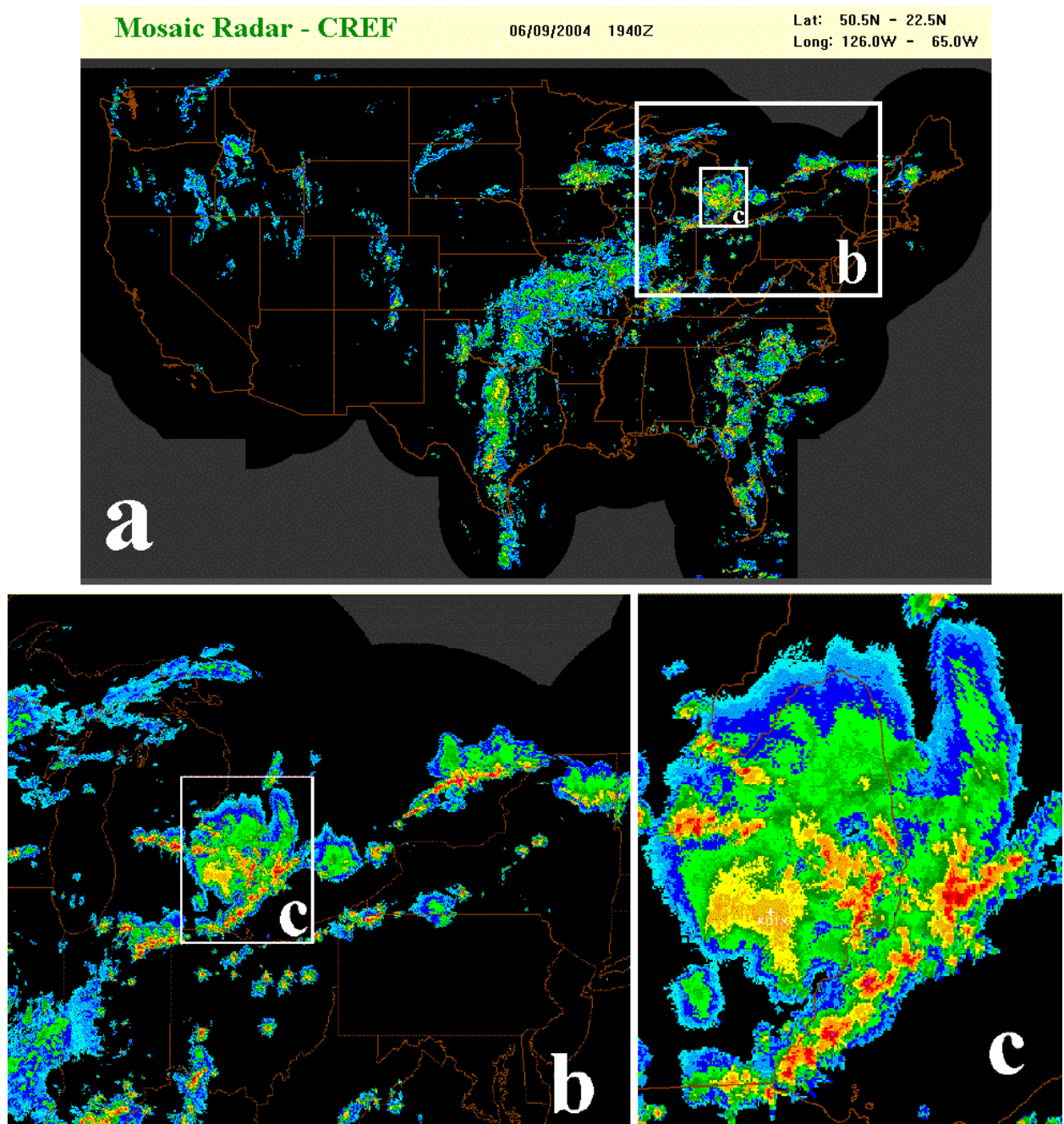


Figure 11 An example composite reflectivity image from the NMQ 3D mosaic (a) and two zooming-in images for smaller regions (b and c).

#### **04.6.14.9 Implement the NCAR REC algorithm in the pre-process for 3D multi-radar mosaic.**

Initial code for components of the NCAR Radar Echo Classifier (REC)\* algorithm has been developed. About 200 volume scans of data from radars in different geographical regions were collected for the REC performance case analysis. The cases include various examples of ground clutter, anomalous propagation (AP), birds and insects, and other non-meteorological echoes such as chaff. The REC algorithm will be tested using these analysis cases in the next quarter.

\*REC, Kessinger et.al. 2003: The radar echo classifier: a fuzzy logic algorithm for WSR-88D, *3<sup>rd</sup> Conference on Artificial Intelligence Applications to the Environmental Science*, AMS, 9-13 February 2003, Long Beach, CA)

#### **04.6.14.10 Test the REC using archived data/cases.**

(This task starts at 1 July 2004.)

#### **04.6.14.11 Continue to develop the prototype 4-D dynamic data updating system. Start 1 Jan 04.**

A preliminary real-time 4D dynamic grid (4DDG) prototype has been developed. Figures 12 and 13 show the conceptual models of the 3D mosaic and the 4D dynamic grid. In the 3D mosaic (Fig. 13), reflectivity data from different radars are combined onto a unified Cartesian grid at regular clock times. The data are ingested as per full volume scans and time differences between different volume scans are neglected. The Cartesian grid is re-initialized every time when the 3D mosaic module is executed.

In the 4DDG, the reflectivity data are ingested continuously as each new tilt arrives (Fig. 13). The Cartesian grid is initialized only once at the beginning time when the 4DDG module begins. The 3D grid is continuously updated as new tilt of data becomes available. The 4DDG module runs in 'forever' mode instead of on discrete clock times.

The 4D mosaic system provides a more rapid update depiction of storm structure and evolution than the 3D mosaic system since the 4D mosaic grid updates based on the time scale of an individual tilt instead of the time scale of a complete volume scan. This is especially evident in regions with relatively dense radar coverage. The 4D radar mosaic technique will be suitable for the analysis of rapidly updating radars such as phased array radars. The rapid update NMQ 4-D mosaic can provide users, especially those from the aviation community, more timely depiction of a storm structure and aerial distribution than the 3D mosaic. However, the 4D mosaic system is relatively computationally expensive and is still in refinement.

It has been proposed to delay the rest of the 4DDG research, testing and development for the current year to a later year so that efforts can be focused on improving the NMQ 3D mosaic (e.g., better reflectivity QC, hole-filling between bottoms of the lowest radar beams and the ground, integration of TDWR data into the NMQ 3D mosaic, etc). Additionally, resources are



required for generating 3D mosaic grid for past events based on requests from other AWRP PDTs (e.g., new tasks 04.6.14.11A, 04.6.14.12A, and 04.6.14.13).

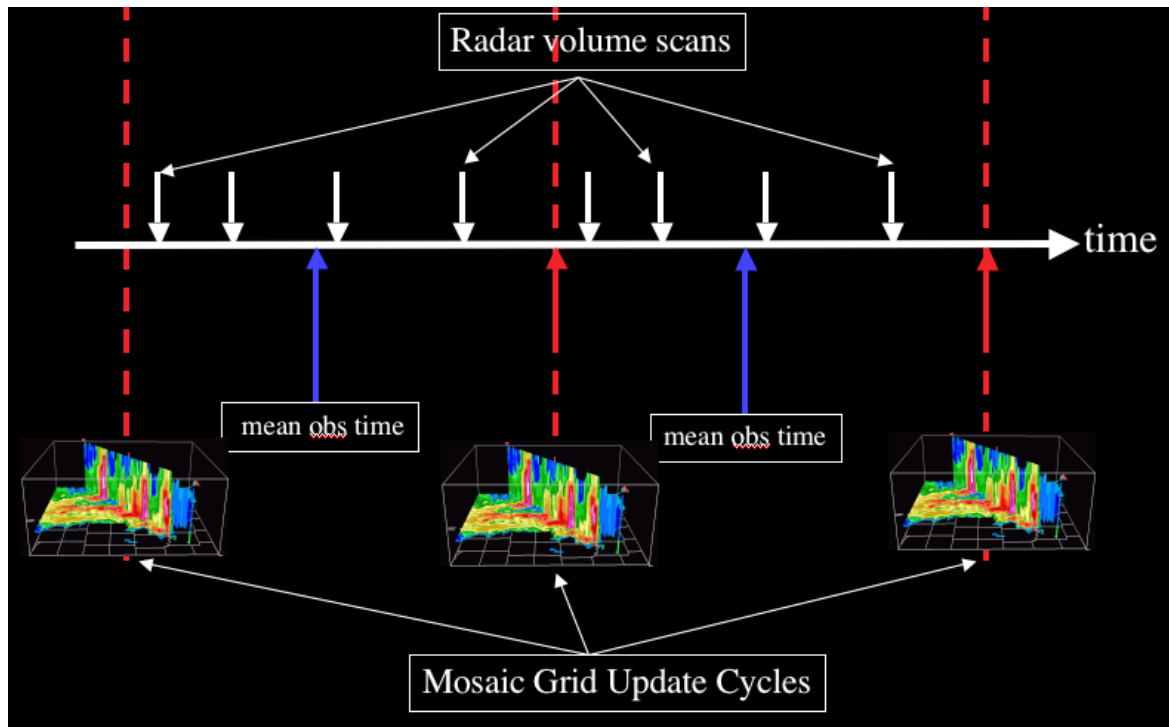


Figure 12 An illustration of the 3D mosaic update cycles.

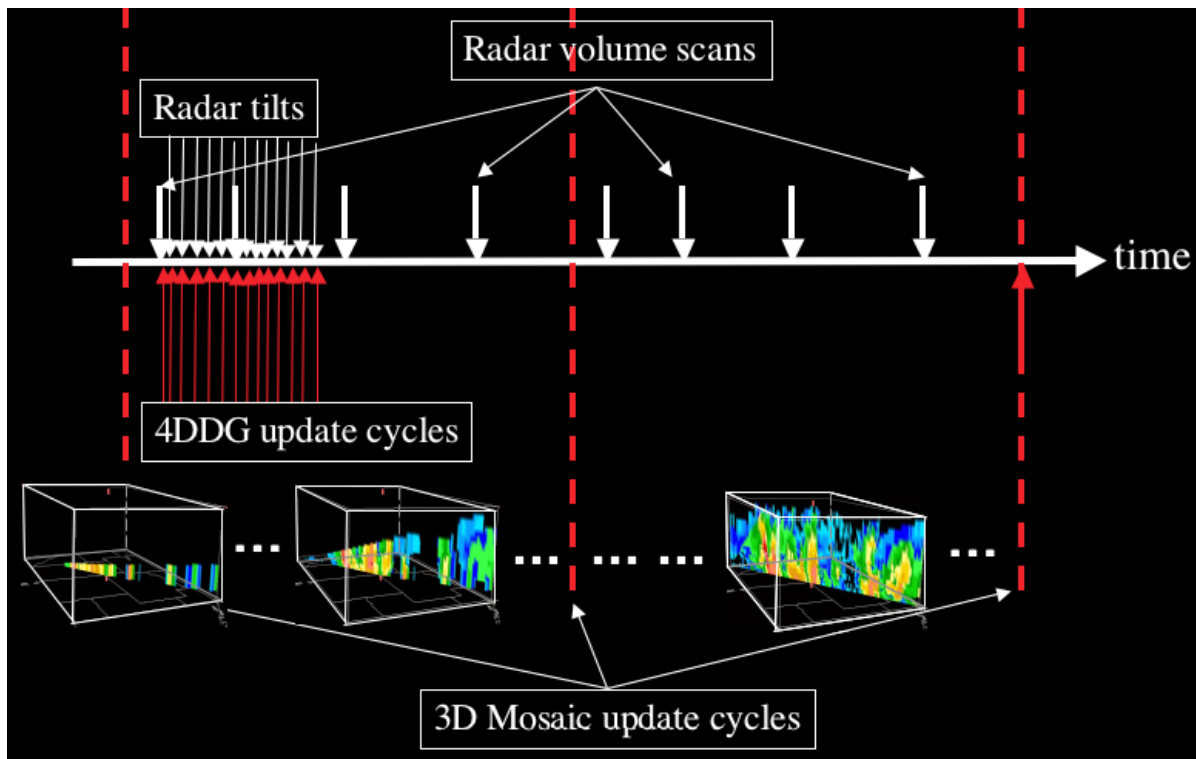


Figure 13 An illustration of the 4D dynamic grid update cycles.

#### **04.6.14.12 Testing the prototype 4-D dynamic grid using WSR-88D and TDWR data with a tilt-based update cycle.**

(This task was planned to start at 1 July 2004. But it is now postponed to a later year because of the new tasks 04.6.14.11A, 04.6.14.12A, and 04.6.14.13.)

#### **04.6.14.11A Collect level-2 data from NCDC for all radars that cover the IHOP 2002 domain for the IHOP 2002 cases specified by the Model Development and Enhancement PDT. Start 1 June 04.**

The activities for this quarter include retrieving level-II data from NCDC for 49 radars covering the IHOP domain (tiles 4 and 5 in the NMQ mosaic grid, Fig. 2) for an event occurred on 15-16 June 2002. Total of 33 radars are found to have data for the specific time period (18Z on 15 June to 11Z on 16 June 2002). About 11GB of level-II data were retrieved from NCDC.

#### **04.6.14.12A Process the level-2 data for AP and clutter removal. Start 15 June 04.**

The radar data collected for the IHOP event (04.6.14.11A) have been processed for reflectivity quality control to remove AP and other non-meteorological echoes.

#### **04.6.14.13 Create reference data for the IHOP mosaic grid. Setup scripts and generate 3D mosaic grid for all IHOP 2002 cases. Start 1 July 04.**

The reference data for the IHOP domain are the same as the mosaic reference data for tiles 4 and 5 in the NMQ 3D mosaic grid (Fig. 2). Mosaic scripts that were used for creating CIWS domain 3D mosaic grid were modified. The new scripts are more configurable and more general than the old ones. The new scripts are used to create the 3D mosaic grid for the IHOP event specified by the MDEPDT and the mosaic grid data have been delivered to the MD&E PDT.